Climate change made weather conditions leading to deadly South Korean wildfires about twice as likely

Authors

Clair Barnes, *Centre for Environmental Policy, Imperial College, London, UK*
June-Yi Lee, *Research Center for Climate Sciences, Pusan National University & Center for Climate* Physics, *Institute for Basic Science, Busan, Republic of Korea*
Young-Min Yang, Department of Environment & Energy/School of Civil, Environmental Resources and Energy Engineering/Soil Environment Research Center, Jeonbuk National University, Republic of Korea
Ye-Won Seo, Center for Climate Physics, Institute for Basic Science, Busan, Republic of Korea
Jeong-Eun Yun, Research Center for Climate Sciences, Pusan National University
Wenchang Yang, *Department of Geosciences, Princeton University, Princeton, NJ 08544, USA*
Seongwoo Jo, *Department of Landscape Architecture and Rural Systems Engineering, College of Agriculture and Life Sciences, Seoul National University*
Theodore R. Keeping, *Leverhulme Centre for Wildfires, Environment and Society, Imperial College, London, UK & School of Archaeology, Geography and Environmental Science, University of Reading, UK*
Maja Vahlberg, *Red Cross Red Crescent Climate Centre, The Hague, the Netherlands; Swedish Red Cross, Stockholm, Sweden (based in Ubmeje/Umeå, Sweden)*
Karina Izquierdo, *Red Cross Red Crescent Climate Centre, The Hague, the Netherlands (based in Mexico City, Mexico)*
Friederike Otto, *Centre for Environmental Policy, Imperial College, London, UK*

Review authors

Ben Clarke, *Centre for Environmental Policy, Imperial College, London, UK*
Sjoukje Philip, *Royal Netherlands Meteorological Institute (KNMI), De Bilt, The Netherlands*
Roop Singh, *Red Cross Red Crescent Climate Centre, The Hague, The Netherlands (based in New Jersey, USA)*
Emmanuel Raju, *Copenhagen Centre for Disaster Research, Global Health Section, Department of Public Health, University of Copenhagen, Copenhagen, Denmark; African Centre for Disaster Studies, North-West University, South Africa*

Main findings

- The fires particularly impacted areas where forests border residential, industrial, and heritage sites, which are crucial for risk reduction and land-use planning. Many of the affected people were older adults or individuals with limited mobility, especially in rural and peri-urban areas, making evacuation difficult.
- Even in today's climate, that has warmed by 1.3℃ due primarily to the burning of fossil fuels, the combination of high temperatures, low humidity and high wind speeds (HDWI) observed over the 5 days following March 22nd, when the fires broke out, was very unusual. In the current climate they are expected on average about once every 300 years.
- However, independent of how the HDWI is calculated, based on weather observations, the event would have been extremely rare if the climate hadn't warmed and the intensity of the peak 2025 March HDWI is about 25% more intense in today's climate compared to the cooler pre-industrial climate.
- To determine the role of climate change in this observed trend we combine the observation-based estimate with climate models. Most climate models also show an increase in the recent past, but weaker than the observed trend. Combining both, we find an increase of about 15% in the intensity of the HDWI and a doubling in likelihood. An increase of similar magnitude is observed in data from 9 weather stations in the region most affected by the fires.
- We further estimate how the peak March HDWI would change in a 1.3℃ warmer climate from today, that is 2.6℃ above pre-industrial and estimated by around 2100 under current policies. We find that all climate models project a further increase in the peak March HDWI with continued warming of about 5% in intensity and a further doubling of the likelihood. This is stronger than the change simulated by the models alone up until today, suggesting that the observed trend is indeed attributable to human-induced climate change but has not emerged in all models yet.
- We also analysed potential changes in the 5-day maximum temperatures in March, finding that while rare in today's climate, the return time of 75 years is not as exceptional as for the combined index. The changes in both observation-based products and models are stronger than in the HDWI, even though the climate models again show a much lower trend than observations. This suggests that the trend in the HDWI is primarily driven by the strong increase in temperature, but that the extremeness of this year's event, with a return time of more than 300 years in today's climate, is not just due to the high temperatures, which only have a return time of 75 years.
- We further analyse the rainfall in the months preceding the outbreak of the fire. Here we find a slight drying trend in the observation-based products as well as most weather stations in the country. However, this drying is not represented in climate models, which may be due to Korea's complex geography as a relatively small

landmass surrounded by ocean, as well as rainfall which experiences long-term decadal changes. Thus, in contrast to the warming and changes in fire weather, we cannot attribute it to human-induced climate change or natural variability.

- South Korea has planted billions of trees since the 1970s to reverse historic deforestation, improve biodiversity, reduce soil erosion, absorb carbon emissions and provide numerous social and cultural benefits. This year's fires have renewed concerns about the effect of tree-planting on wildfire risk, with continuous forest cover resulting in high fuel loads and increased fire risk. While afforestation provides many benefits, the fuel loads near human settlements need to continue to be carefully managed to mitigate dangerous fires, particularly as climate change increases the likelihood of intense fire-prone weather conditions.
- South Korea has made significant progress in wildfire detection, suppression, and early warning. As fire seasons become longer and more intense, there is a growing opportunity to build on these strengths by further aligning wildfire preparedness with infrastructure, land-use, and emergency planning frameworks.

1 Introduction

In March 2025, southeastern Korea experienced its most destructive wildfire season on record. More than a dozen fires broke out between March 22nd and 23rd and spread rapidly over the following days. With 32 casualties, the fires are South Korea's deadliest wildfires on record, additionally injuring 45 people, and displacing about 37,000 residents (AFP, 2025). Most victims were in their 60s and 70s. Uiseong was hardest hit, with 26 deaths, while four occurred in Sancheong. Around 5,000 buildings, including homes, factories, and farms, were destroyed (McGrath, 2025). Over 100,000 hectares burned - shattering the previous record (since 2000) of 26,000 ha in a year (KFS, 2025). Human activities contributed to the ignition of most events (CNN, 2025); however, hotter and drier conditions, accompanied by stronger-than-normal winds, facilitated the rapid spread of fires across regions of continuous vegetation.

For the last 10 years (2014~2023), the costliest disasters in South Korea have been caused by wildfires. The economic cost of wildfires in 2022 was approximately 1.2 trillion won, accounting for about 17% of the total economic cost due to disasters (Ministry of the Interior and Safety, 2024). This cost is approximately twice that of other natural hazards, including heavy rainfall, floods, typhoons, strong winds, and heavy snow, in 2022. The economic cost of wildfire in March 2025 is expected to be much larger than that in 2022.

The fires disproportionately affected rural and peri-urban populations, particularly in so-called Wildland-Urban Interface (WUI) zones, where residential areas intermix with dense forest cover. Uiseong, one of the hardest-hit areas, saw the destruction of Gounsa Temple - originally built in 618 AD - and damage to 30 registered cultural heritage sites, including relics from the Joseon Dynasty (AFP, 2025; Sang-Soo, 2025).

Wildfires are a common occurrence at this time of year in this region, due to increasing Spring temperatures, relatively low rainfall compared to the hotter summer months, strong wind, and increasing risks of human-induced ignition (Sung et al., 2010; Kim et al., 2025).

This year, wildfire-prone conditions were exacerbated by extremely warm and dry weather conditions. From March 22nd to 26th the daily maximum temperature averaged over southeastern Korea reached up to 25 °C, more than 10°C higher than March climatology. There was no rainfall, and the daily minimum relative humidity reached about 20% from the 21st to the 25th. The extremely warm and dry conditions were accompanied by a strong high pressure in the south and a low pressure in the North, leading to strong westerly winds in southeastern Korea. The maximum wind speed at the key locations was as high as 25 m/s on March 25 (Forest.Go.KR, 2025; N News, 2025), contributing to the rapid spread of the fires.

1.1 Wildfires in Korea

In South Korea wildfires occur mainly during the spring season, with the highest number of occurrences in March, followed by April; they occur particularly in the East, such as the provinces of Kyungbuk and Gangwon, which are exposed to the highest inland winds (Korea Meteorological Administration, 2018). South Korea has a monsoon climate characterized by cold, dry winters and hot, wet summers. During March and April, meteorological conditions are most favorable for the occurrence of wildfires. During this spring period, surface temperatures increase rapidly, while rainfall remains relatively low, resulting in dry soil and vegetation. Synoptic disturbances during the period are often characterized by either a high in the west and a low in the east or a high in the south and a low in the north, leading to strong westerly or southwesterly winds that further increase the risk (Lee et al., 2022; Yum et al., 2024). In addition to meteorological factors, environmental and human factors also contribute to the occurrence of wildfires. In South Korea, more than 60% of the country's land is covered by forests, 11% of which are at the Wildland-Urban Interface (WUI). About 30% of forest fires from 2016 to 2022 occurred in the WUI in South Korea (Jo et al., 2013). Ignition of wildfires is primarily associated with human activities rather than natural ignition, such as lightning strikes. During March and April, the number of hikers increases, which leads to an increased risk of fire ignition. Recent studies, e.g. Kim et al., (2025) and Chang et al., (2024), have found that the fire season is becoming longer, and consequently the burned area is increasing.

1.2 The effect of climate change on wildfire risk

The climatological fire weather season in South Korea begins in early spring (March) and extends through the autumn. However the primary season when most fires occur is spring, when humidity and fuel moisture is lower, reducing the ignition barrier and allowing for more intense spread. There are usually 500–900 wildfire events annually, typically burning an area of 1,000–4,000 hectares. In recent years, the number of wildfire events has increased by approximately 30%, reaching up to 1,200 events per year, and an increase in burned area has been observed, particularly since 2019 (see Figure 1.1).

The previous worst fire season was in 2000 when the total burned area reached about 26,000 hectares, followed by 2022 with about 25,000 hectares burned.

The analysis of the role of climate change for wildfire risk in Korea in the IPCC is comparably superfluous, but assessed to be increasing with medium confidence (Ranasighe et al., 2021). This is corroborated by more recent studies, e.g. an analysis of the 2022 fires suggests that the winter climate in South Korea is changing from relatively cold and wet to comparably warm and dry due to climate change (Chang et al., 2024). However this study, and others cited within, base their analysis on historical data, without an explicit attribution component. While there is no doubt that the increase in temperatures is driven by human-induced warming (see, e.g., Seneviratne et al., 2021, Seong et al., 2020), the drivers of the observed drying are less clear. In contrast to many other regions in the world, the IPCC-assessed studies evaluating present day changes in rainfall in East Asia disagree with each other and show both increases and decreases driven by human-induced climate change, depending on the exact region and season but also methods used (Seneviratne et al., 2021). Kim et al., (2025) analysed mechanisms behind observed drying trends in East Asia - including South Korea - and found that they differed depending on the region; some were dynamically driven, while others resulted from thermodynamic processes in the vertical atmosphere. The complexity of these drivers means that hurdles for adequate climate models to study these trends are very high. Climate models with typical horizontal resolution have shown limitations in representing physical processes and complex terrain effects that are crucial for reproducing East Asian monsoon climate (Liu et al., 2023). Kwon et al., (2025) found that the vertical representation of the atmosphere in climate models played an important role in accurately reproducing rainfall in South Korea. While that study focuses on heavy rainfall, the conclusions explicitly include rainfall in general; thus, conclusions about changing rainfall patterns in South Korea due to climate change are likely to be hampered at this point in time by a lack of high resolution modelling available for attribution studies. In addition, rainfall in Korea is influenced by decadal variability that impedes the disentangeling of trends driven by climate change from those driven by large scale modes of variability (Kim et al., 2015, Om et al., 2018, Lee et al., 2017, Lee et al., 2019, Lee et al., 2023).

1.3 Event Definition

March 2025 saw a number of extreme wildfires affecting the southeast of Korea, affecting the North Gyeongsang, South Gyeongsang and Ulsan provinces. The largest wildfires occurred in North Gyeongsang, with wildfires affecting five districts (Uiseong, Andong, Cheongsong, Yeongyang and Yeongdeok) and burning 99,300 ha according to Korea Forest Service data. South Gyeongsang and Ulsan experienced burned areas of 3,400 ha (in the Sancheong and Hadong districts) and 1,200 ha (in Ulju) respectively. The wildfires began on March 21st and were fully contained by March 30th, with the total burned area being 103,876 ha (Korea Forest Service, 2025). These burned areas shatter previous burned area records in South Korea, with the previous annual record in 2000 being 26,000 ha over the entirety of the country (Korea Forest Service, 2024).

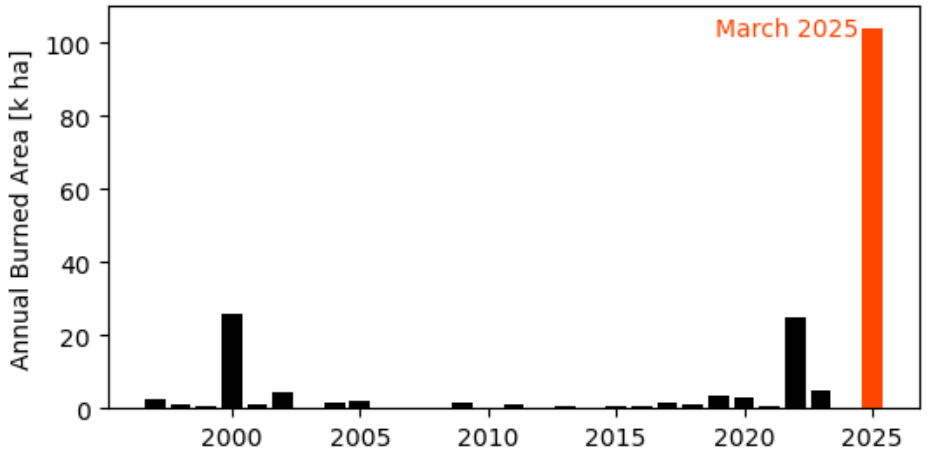

Figure 1.1: *Time series of annual area burned taken from Korea Forest Service Forest Fire Statistical Yearbooks from 1997-2024 (Korea Forest Service, 2024), with burned area in March 2025 (Korea Forest Service, 2025) added for context.*

Fire weather is the meteorological component of the wildfire hazard, which in conjunction with live and dead vegetation availability as well as ignition sources drive wildfire events (Pausas and Keeley, 2021). Fire weather consists of longer term antecedent fuel moistening and drying effects, which control the flammability of bulkier dead fuels. We consider the lows in February-March precipitation as a proxy for bulk fuel moisture, an appropriate time period given that the bulkiest fuels take up to 1000 hours (about 40 days) to dry (Fosberg et al., 1981). Wildfires spread more quickly when very fine fuels are extremely dry and ignitable, which occurs in windy conditions with high atmospheric evaporative demand – with wind further contributing to the rate of wildfire spread and consequent suppressibility (Srock et al., 2018). Vapour pressure deficit (VPD) defines the additional amount of moisture the atmosphere is capable of holding, and thus its maximum relates to the instantaneous drying demand on rapidly drying fuels and the maximum fire risk; and has been found to be the strongest meteorological explanatory factor for wildfire behaviour across environments in the United States (Williams et al., 2015; Sedano and Randerson, 2014). The hot-dry-windy index (HDWI) (Srock et al., 2018) captures fuel flammability and wildfire spread rate effects by multiplying maximum daily wind speed and maximum daily VPD. This index has the benefit of not being tuned to specific environmental and vegetation conditions, such as the more sophisticated Canadian Fire Weather Index which was developed empirically for a specific forest type (Van Wagner et al., 1987). Wildfire growth is in part determined by the length of the existing fire perimeter, meaning that multiple consecutive days of highly flammable conditions can result in much more severe overall wildfire events.

The event definitions used in this study are defined below and summarised in Table 2.1.

1.3.1. Hot-dry-windy index (HDWI)

To capture the fire weather conditions at the time the fires broke out, we take a 5-day running mean of the mean HDWI over South Korea, and analyse trends in March maxima of this index (henceforth denoted HDWI5x). This 5-day average captures the persistent extremes required for multiple days of rapid wildfire spread, and reflects the extremeness of the conditions at the time of the fires (Figure 1.2). Trends in HDWI5x are relatively homogeneous across Korea (see Figure A1.1), so we are confident that the trends in this univariate index reflect real trends in fire conditions across the country.

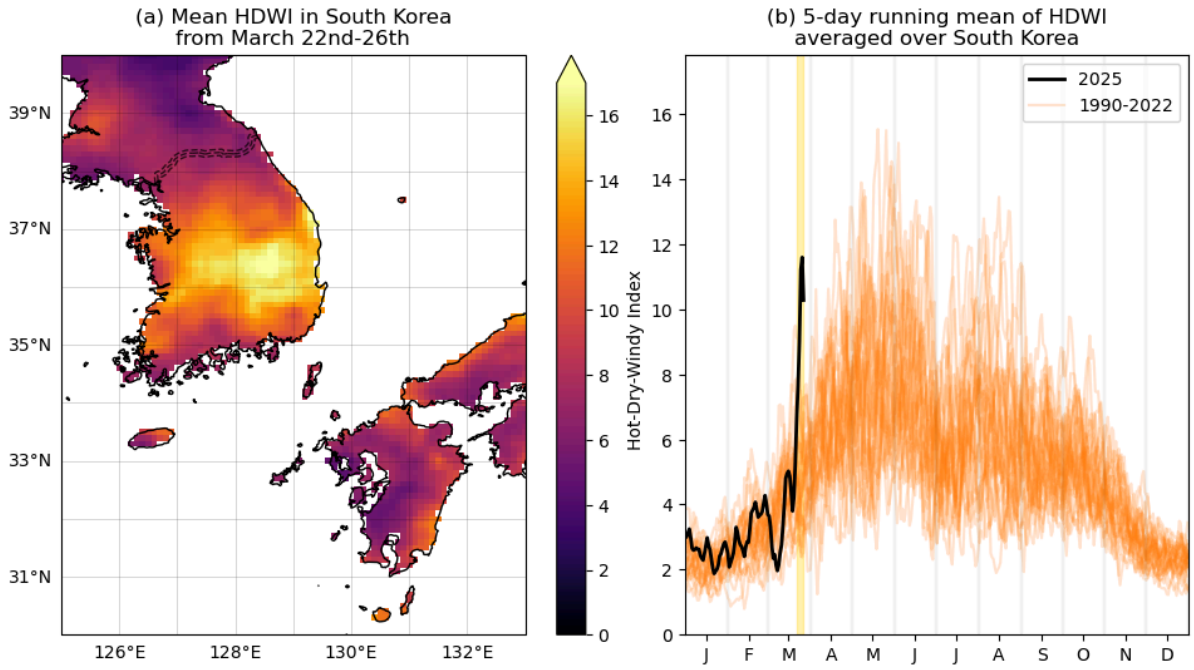

Figure 1.2: *(a) Map of mean HDWI from March 22nd-26th. (b) Five-day running mean of HDWI over South Korea during 2025 (black line) and recent climatology (orange lines). The period from March 22nd-26th is highlighted in yellow.*

Trends in HDWI in this region are closely correlated with trends in daily maximum temperatures (see Section 3.1.2) and so we also attribute changes in the warmest 5-day period each March. We take a 5-day running mean of the mean daily maximum temperatures over South Korea, and analyse trends in March maxima of this index (henceforth denoted TX5x).

1.3.2. February-March rainfall

Typically February and March are slightly wetter than the winter months (December-January), but with the exception of one day, during the spring of 2025 South Korea received very little rain, leading to high availability of dry fuel. To reflect the dry conditions in the months preceding the fires, we examine trends in accumulated February to March precipitation over the whole of Korea (Figure 1.3), henceforth denoted PR-FM.

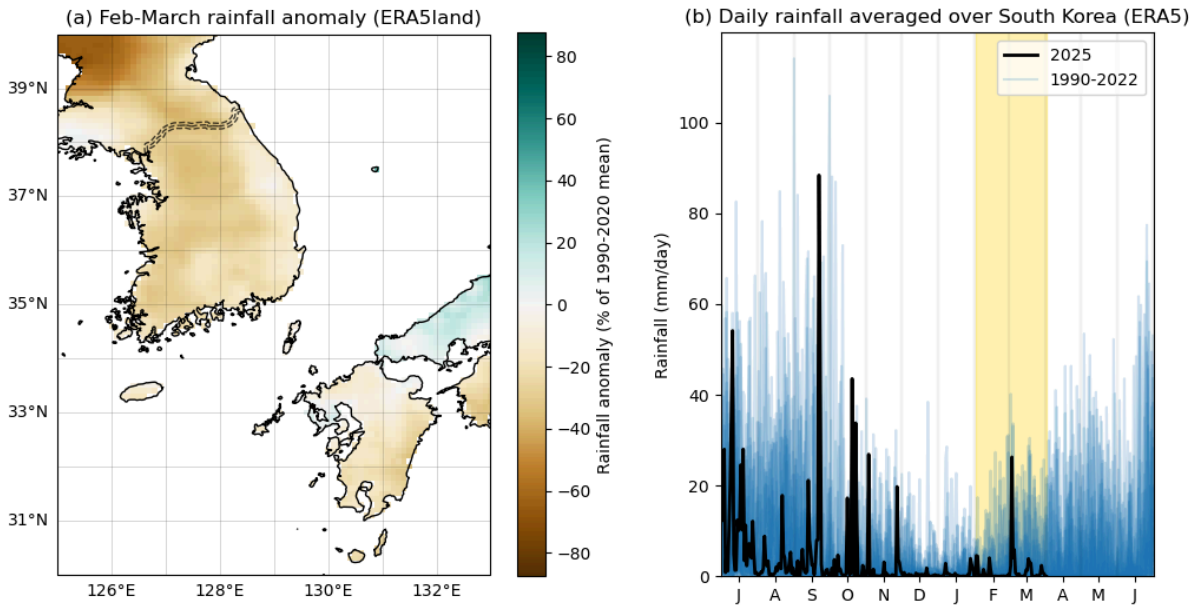

Figure 1.3: *(a) Map of February-March 2025 rainfall anomaly, expressed as a percentage of the 1990-2020 climatology. (b) Average daily rainfall over South Korea during 2024-25 (black line) and recent climatology (blue lines). February and March are highlighted in yellow.*

2 Data and methods

In this report, we study the influence of anthropogenic climate change by comparing the likelihood and intensity of similar weather conditions at present with those in a 1.3°C cooler climate. We also extend this analysis into the future by assessing the influence of a further 1.3°C of global warming from present. This is in line with the latest Emissions Gap Report from the United Nations Environment Programme, which shows that the world is on track for at least 2.6°C temperature rise given currently implemented policies (UNEP, 2024).

2.1 Observational data

We first use observational and reanalysis data to estimate the return period of a similar event in the present day and to assess the historical trends with increasing GMST. The datasets used are as follows:

ERA5-Land (Muñoz-Sabater et al., 2021) produced by the European Centre for Medium-Range Weather Forecasts. This product is a replay of the land component of the ERA5 climate reanalysis with a finer spatial resolution of 0.1° (~9km grid spacing), at hourly time steps from 1950 to 5 days before the current date. The land model used is the tiled ECMWF Scheme for Surface Exchanges over Land incorporating land surface hydrology (H-TESSEL).

Station data from nine locations within the worst-impacted region of Korea were obtained from the Korea Meteorological Administration.

As a proxy for anthropogenic climate change we use the (low-pass filtered) global mean surface temperature (GMST), where GMST is taken from the National Aeronautics and Space Administration (NASA) Goddard Institute for Space Science (GISS) surface temperature analysis (GISTEMP, Hansen et al., 2010 and Lenssen et al. 2019).

2.2 Model and experiment descriptions

We use three multi-model ensembles from climate modelling experiments using very different framings (Philip et al., 2020): Sea Surface temperature (SST) driven global circulation high resolution models, coupled global circulation models and regional climate models.

CMIP6. This consists of simulations from 28 participating models with varying resolutions. For more details on CMIP6, please see Eyring et al., (2016). For all simulations, the period 1850 to 2015 is based on historical simulations, while the SSP5-8.5 scenario is used for the remainder of the 21st century.

HighResMIP SST-forced model ensemble (Haarsma et al. 2016), the simulations for which span from 1950 to 2050. The SST and sea ice forcings for the period 1950-2014 are obtained from the 0.25° x 0.25° Hadley Centre Global Sea Ice and Sea Surface Temperature dataset that have undergone area-weighted regridding to match the climate model resolution (see Table B). For the 'future' time period (2015-2050), SST/sea-ice data are derived from RCP8.5 (CMIP5) data, and combined with greenhouse gas forcings from SSP5-8.5 (CMIP6) simulations (see Section 3.3 of Haarsma et al. 2016 for further details).

AM2.5C360 (Yang et al. 2021, Chan et al. 2021) and **FLOR** (Vecchi et al. 2014) climate models developed at Geophysical Fluid Dynamics Laboratory (GFDL).
The AM2.5C360 is an atmospheric GCM based on that in the FLOR model (Delworth et al. 2012, Vecchi et al. 2014) with a horizontal resolution of 25 km. Ten ensemble simulations of the Atmospheric Model Intercomparison Project (AMIP) experiment (1871-2021) are analysed. These simulations are initialised from ten different pre-industrial conditions but forced by the same SSTs from HadISST1 (Rayner et al. 2003) after groupwise adjustments (Chan et al. 2021), as well as the same historical radiative forcings. The FLOR model, on the other hand, is an atmosphere-ocean coupled GCM with a resolution of 50 km for land and atmosphere and 1 degree for ocean and ice. Three ensemble simulations from FLOR are analysed, which cover the period from 1860 to 2100 and include both the historical and RCP4.5 experiments driven by transient radiative forcings from CMIP5 (Taylor et al. 2012).

AWI-CM3 (the Alfred Wegener Institute Climate Model version 3.0) is a coupled GCM using the ECMWF IFS TCo atmospheric grids, and used here at 31 km horizontal resolution (Streffing et al., 2022). The ocean dynamics are simulated by FESOM2 (Finite-volumE Sea ice–Ocean Model) and atmospheric dynamics simulated by OpenIFS (CY43R3). The data used in this study consists of a simulation from 1950-2070, using historical forcings from 1950 to 2014 and transient greenhouse and

aerosol forcing of the emission-intensive SSP5-8.5 greenhouse gas concentration scenario (Moon et al., in press).

2.3 Calculation of VPD and HDWI

Ideally, the vapour-pressure deficit is first calculated from hourly temperature(T) and dewpoint temperature (T_d) or hourly temperature (T) and relative humidity (R) using equation (1) or (2); the daily maximum of the hourly VPD is then multiplied by the daily maximum sustained wind speed to give the daily HDWI (Srock et al., 2018).

$$VPD = \exp\frac{17.25T}{243.04+T} - \exp\frac{17.25T_d}{243.04+T_d} \quad (1)$$

$$VPD = \exp\frac{17.25T}{243.04+T}(1 - R) \quad (2)$$

However, hourly-resolution data is not available for most climate models. Instead, we use equation (2) with R denoting the daily minimum relative humidity and T the daily maximum temperature. Figure 2.1 shows the time series of VPD computed using both methods; the calculated values are extremely similar and the trends are essentially identical, so we are confident that using daily data to calculate the HDWI will not impact the results of the analysis.

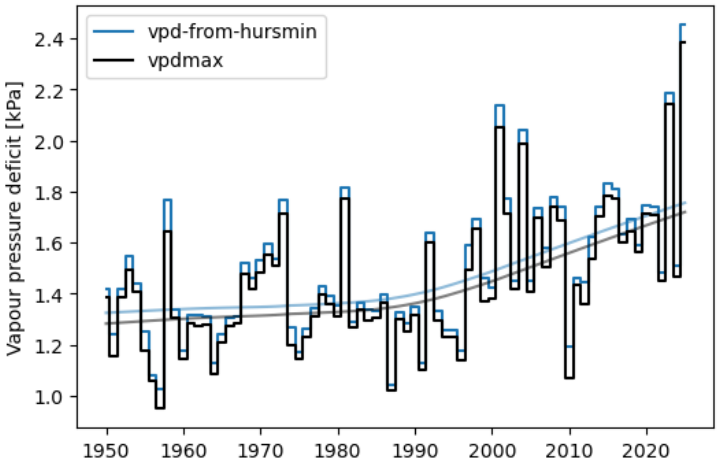

Figure 2.1: *Time series of VPD computed using hourly temperatures (black) and minimum daily relative humidity and maximum daily temperature.*

2.4 Statistical methods

Methods for observational and model analysis and for model evaluation and synthesis are used according to the World Weather Attribution Protocol, described in Philip et al., (2020), with supporting details found in van Oldenborgh et al., (2021), Ciavarella et al., (2021), Otto et al., (2024) and here. The key steps, presented in Sections 3-6, are: (3) trend estimation from observations; (4)

model validation; (5) multi-method multi-model attribution; and (6) synthesis of the attribution statement.

For each time series we estimate the parameters of a statistical model in which the index depends on the GMST. This model is then used to estimate the return period and intensity of the event under study for the 2025 GMST and for a 1.3°C cooler counterfactual climate: this allows us to compare the expected intensity and frequency of similar events now and in the preindustrial past (1850-1900, based on the Global Warming Index), by calculating the probability ratio (PR; the factor-change in the event's probability) and change in intensity of the event.

Table 2.1 summarises the time series used in this report, and the statistical distributions and assumptions used to model the changes due to each covariate.

Index	**Description**	**Distribution**	**Nonstationarity assumption**
HDWI5x	March maximum of 5-day mean of HDWI	GEV	Shift
TX5x	March maximum of 5-day mean of daily maximum temperatures	GEV	Shift
PR-FM	February-March accumulated rainfall	Log-normal	Shift
sfcWindmax1x	March maximum sustained windspeed	GEV	Shift
VPD5x	March maximum of 5-day mean of VPD	GEV	Shift
hursmin5n	March minimum of 5-day mean of relative humidity	GEV	Shift

Table 2.1: *Summary of time series of indices and statistical models used to estimate the influence of different covariates in these metrics.*

Exploratory analysis of the data showed that the February-March rainfall time series is quite skewed (Figure 2.2). To normalise the data, we apply a log transformation; the transformed data is well modelled by a normal distribution (panel b). This approach is used in preference to directly fitting a log-normal distribution because parameter estimation is more numerically stable. The log-transformed precipitation is assumed to shift linearly with GMST (that is, the mean of the distribution changes, while the variance remains constant). Absolute changes in log-transformed precipitation correspond to relative (percentage) changes in raw precipitation.

All of the other indices studied in this report are also assumed to shift linearly with GMST. All parameters are estimated using maximum likelihood.

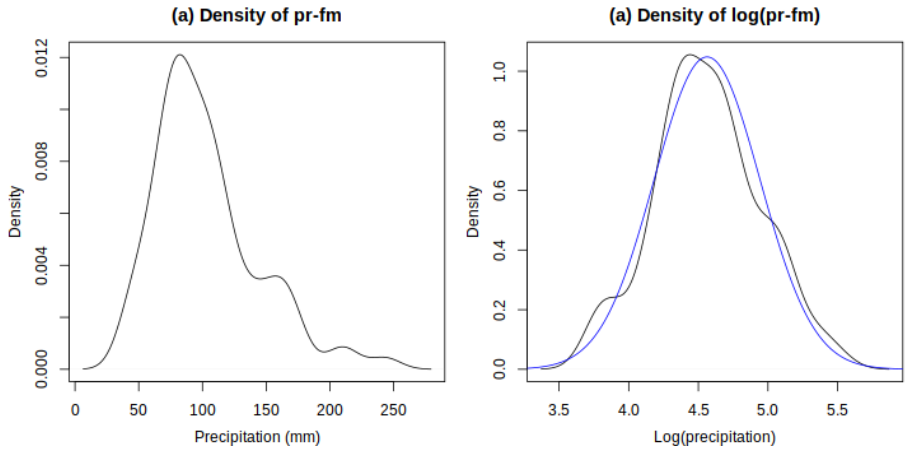

Figure 2.2: *Kernel density estimate of (a) PR-FM and (b) log-transformed PR-FM (ERA5-land). The blue line in panel (b) denotes the density of a normal distribution fitted to the log-transformed data.*

3 Observational analysis: return period and trend

3.1 Trends in HDWI

3.1.1 Trends in gridded reanalysis products

Figure 3.1 shows HDWI5x in the ERA5-land dataset, as a function of time (panel a) and of GMST (panel b). There is a slight dip in HDWI5x from around 1980 to 1995 (corresponding to a GMST anomaly of -1°C to -0.8°C with respect to current levels), but other than this the nonparametric smoothed trend (dashed green line) is fairly linear in GMST, suggesting that the forced trend is relatively well represented by the linear model. In the return level plots (panel c) most of the points representing the observed HDWI5x values lie close to the line representing the expected values, indicating that the model fits the data well; the two most extreme observations, while far from the line, remain within the bootstrapped 95% confidence interval.

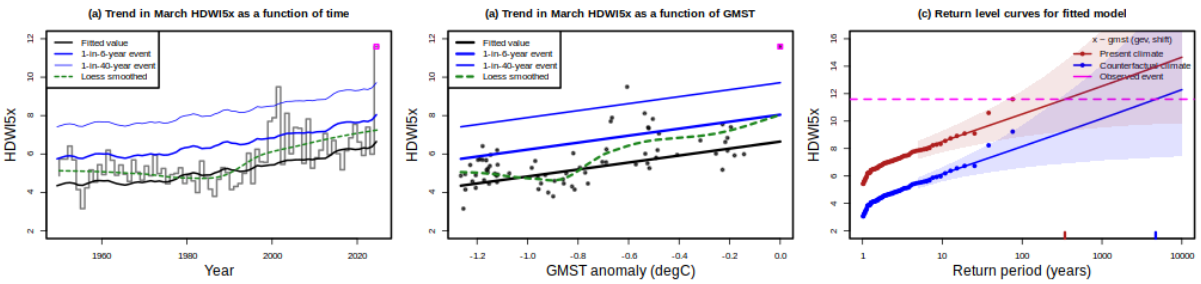

Figure 3.1: *March HDWI5x and fitted linear trends (ERA5-land).* ***(a)*** *Fitted trend in HDWI5x over time; the heavy black line indicates the location of the distribution; blue lines indicate the 6-year and 40-year expected return level; green dashed line is a nonparametric Loess smoother and the pink dot shows HDWI5x in March 2025.* ***(b)*** *as (a), but showing HDWI5x as a function of GMST anomaly with respect to 2025.* ***(c)*** *Expected return levels of HDWI5x over the study region in the 2025 climate (red lines) and in a 1.3C cooler counterfactual climate (blue line), estimated from the statistical model. Shaded regions represent 95% confidence intervals obtained via a bootstrapping procedure. The pink line shows the peak HDWI5x during March 2025. Red and blue ticks at the x axis indicate the estimated return level of March 22nd-26th in the 2025 climate and counterfactual climate.*

The observed maximum daily HDWI5x in 2025 occurred between March 22nd and 26th; according to the fitted model, this event has a return period of around 340 years. Because the conditions were so extreme, and because we only have 75 years of reanalysis data with which to estimate the return period, the uncertainty is very high (95% confidence interval: 67 to infinity); to still represent an extreme event, but better constrain the sampling uncertainty , we use a return period of 100 years in the full attribution analysis.

According to the statistical model, 1.3°C of global warming has increased the intensity of peak March HDWI by around 25% (95% confidence interval: 16-38%) and increased the likelihood of experiencing similarly extreme March HDWI5x by a factor of nearly 14 (95% confidence interval: 3.3 to infinity). These results are summarised in Table 3.1.

	Event magnitude	Return period	Change in HDWI5x	% Change in HDWI5x	Probability ratio
Observed event	11.6	342 (67 - ∞)	**2.4 (1.6 - 3.2)**	**25.6 (16.0 - 37.6)**	**13.7 (3.3 - ∞)**
100-year event	10.9	100	**2.4 (1.6 - 3.2)**	**27.6 (17.3 - 40.1)**	**14.1 (3.6 - ∞)**

Table 3.1: *Summary of fitted model results for March HDWI5x in ERA5-land. Event magnitude; return period of 2025 HDWI5x in the 2025 climate; probability ratio, absolute change in HDWI5x and % change in HDWI5x associated with 1.3°C of global warming. Figures in parenthesis indicate 95% confidence interval obtained via bootstrapping. Statistically significant changes are highlighted in* ***bold****.*

3.1.2 Trends in components of the HDWI

In order to understand the likely factors driving the observed increase in HDWI, we now briefly consider trends in the weather variables that contribute to the index, although no formal attribution is carried out.

Figure 3.2 shows the climatology and 2025 values of each of the components of the March HDWI (as described in Section 1.2, the HDWI is the product of each day's maximum sustained wind speed and vapour-pressure deficit, which can be derived from the daily maximum temperature and daily minimum relative humidity (Srock et al., 2018)). The maximum wind speed peaked for a single day on March 25th (UTC), the day on which the fires spread most rapidly (panel a), while the VPD was unusually high for the whole period of increased fire activity from March 22nd-26th (panel b). Daily maximum temperatures were also unseasonably high during this period (panel c), while the relative humidity was not particularly unusual for the time of year, suggesting that the high VPD that produced such fire-conducive conditions was driven largely by the extreme heat, while the high wind speeds that caused the rapid spread of the fires lasted for a shorter time.

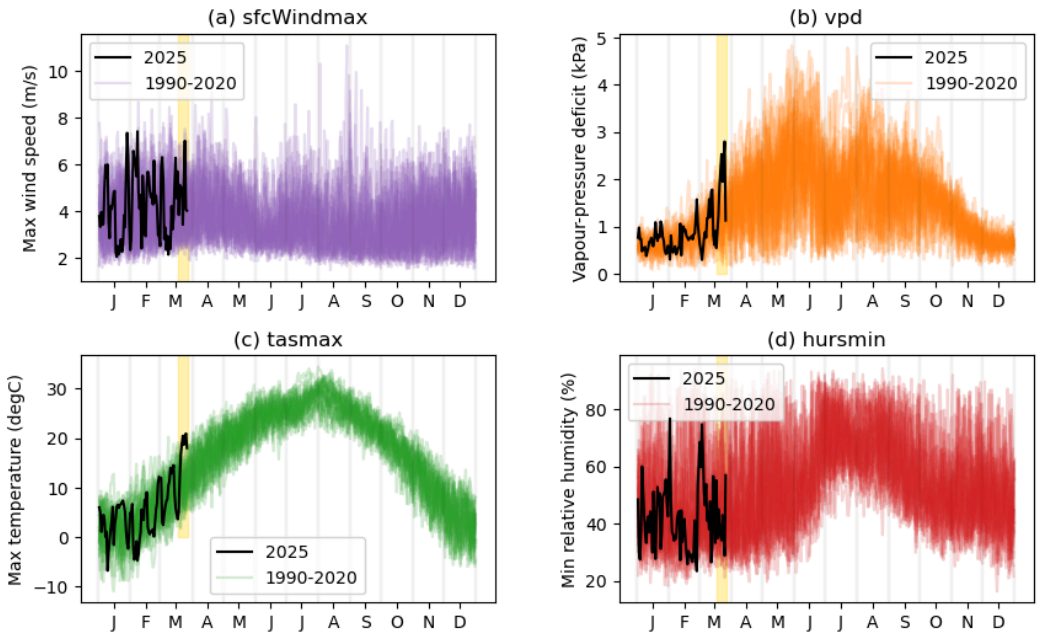

Figure 3.2: *Distribution of HDWI sub-indices averaged over South Korea (ERA5-land). Coloured lines indicate daily values from 1990-2020; black lines indicate 2025 values. The period of the most intense fires (March 22nd-26th) is highlighted in yellow.* ***(a)*** *Maximum sustained wind speed;* ***(b)*** *maximum vapour pressure deficit;* ***(c)*** *maximum temperature;* ***(d)*** *minimum relative humidity.*

Figure 3.3 shows trends in March extrema of the components of the March HDWI. Panel a shows the windiest day each March; apart from a dip in values from 1980-2000, which may explain the low HDWI values noted in Section 3.1.1, no trend is evident. The time series of maximum 5-day VPD and maximum 5-day temperatures are highly correlated (Pearson correlation coefficient: 0.87) and both exhibit a strong upward trend with increasing GMST (panels b & c). Minimum relative humidity is also decreasing as the world warms, but to a lesser extent, and is less correlated with VPD (Pearson correlation coefficient: -0.35), suggesting that the trend in VPD - and therefore in HDWI - is driven largely by increasing temperatures. Because of this strong dependence of the HDWI on daily maximum temperatures, we also evaluate attributable changes in daily maximum temperatures in Section 6. These results are summarised in Table 3.2.

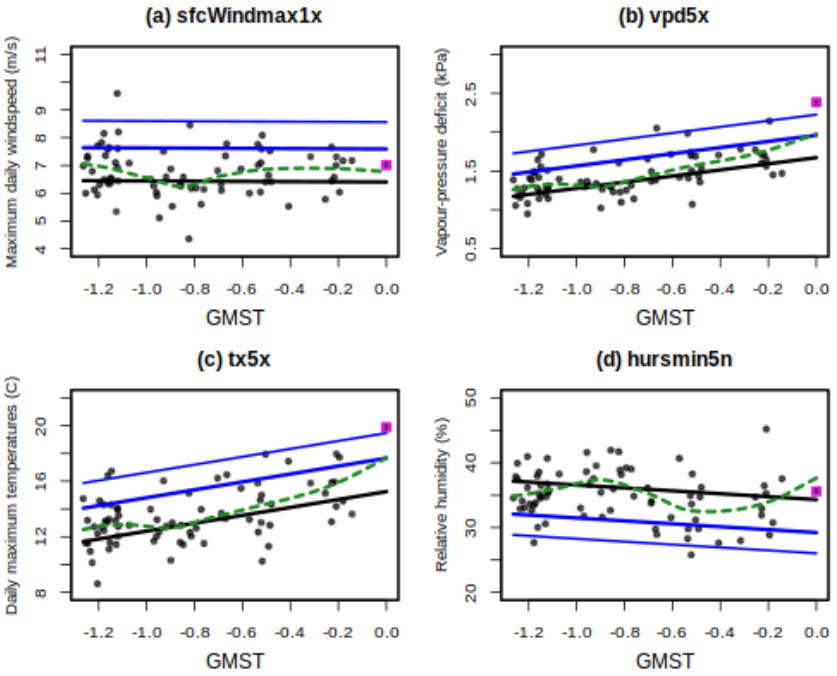

Figure 3.3: *Trends in extrema of sub-indices of HDWI averaged over the study region, as a function of GMST (ERA5-land). Heavy black line indicates the location of the distribution; blue lines indicate the 6-year and 40-year expected return level; green dashed line is a nonparametric Loess smoother and pink dot shows the value of the index from March 22nd-25th 2025 (concurrent with the peak HDWI5x value).* ***(a)*** *Maximum sustained daily wind speed;* ***(b)*** *maximum 5-day vapour pressure deficit;* ***(c)*** *maximum 5-day temperature;* ***(d)*** *minimum 5-day relative humidity.*

Index	Event magnitude	Return period	Change in intensity	Probability ratio
sfcWindmax1x	7.02 m/s	2.78 (1.84, 5.01)	-0.05 m/s (-0.71, 0.58)	0.95 (0.42, 1.95)
vpd5x	2.38 kPa	173 (36, 1547000)	**27.3 % (16.3, 43)**	**4411 (9.6, ∞)**
tx5x	19.9 °C	75 (18, 13000)	**3.7 °C (1.8, 5.5)**	**∞ (12.2, ∞)**
hursmin5n	35.6 %	1.35 (1.09, 2.01)	-2.92 % (-7.2, 0.5)	1.58 (0.93, 2.8)

Table 3.2: *Summary of fitted model results for sub-indices of HDWI5x. Recorded value; return period of 2025 HDWI5x in the 2025 climate; probability ratio, absolute change in HDWI5x and % change in HDWI5x associated with 1.3°C of global warming. Figures in parenthesis indicate 95% confidence interval obtained via bootstrapping. Statistically significant changes are highlighted in* ***bold****.*

3.1.3 Trends in station data

To check the robustness of our results, we evaluate the trends in ERA5-land against station data from nine stations in the area most affected by the wildfires (Figure A2.3). Time series of annual HDWI5x (using VPD calculated from daily maximum temperature and daily minimum relative humidity) are shown in Figure 3.4. In most stations, HDWI is increasing and the trends are similar to those seen in the corresponding grid cell in ERA5-land, although the magnitude of the HDWI is lower in the gridded product; however, one station (Gumi) exhibits an opposing trend, with decreasing HDWI. Trends in VPD at all other stations are relatively homogeneous and well represented by ERA5-land (Figure A2.1); several stations, including Gumi, show a strong decrease in maximum wind speeds (Figure A2.2). No quality checks were carried out on the station data, and it is not clear whether this is due to inhomogeneity in the station record or a genuine trend, perhaps due to changes in land use and surface roughness around the stations as found in other parts of the world (Vautard et al., 2019). However, given that ERA5-land replicates the trends in station VPD relatively well and that the trend in HDWI seems to be predominantly associated with changes in VPD, we are confident to base our analysis on ERA5-land.

To summarise the overall trend among the stations, we display the probability ratios and changes in intensity based on the fitted statistical model described in Section 2.4 for each station time series in a synthesis plot (Figure 3.5) similar to the overall synthesis in Section 6. One station shows a decrease in HDWI, while two show no overall trend; the remaining six all exhibit a strong increase in HDWI. The synthesis algorithm (see Section 6) is used to obtain a weighted average of the trend over all nine stations (dark red bars in Figure 3.5); on average, HDWI in the region is estimated to have increased by 13% (95% confidence interval: -17 to 55%) as the world has warmed by 1.3C, and similarly extreme events have become roughly twice as likely (95% confidence interval: 0.12 times as likely to 103 times more likely). These results are visualised in Figure 3.5 and summarised in Table A2.1.

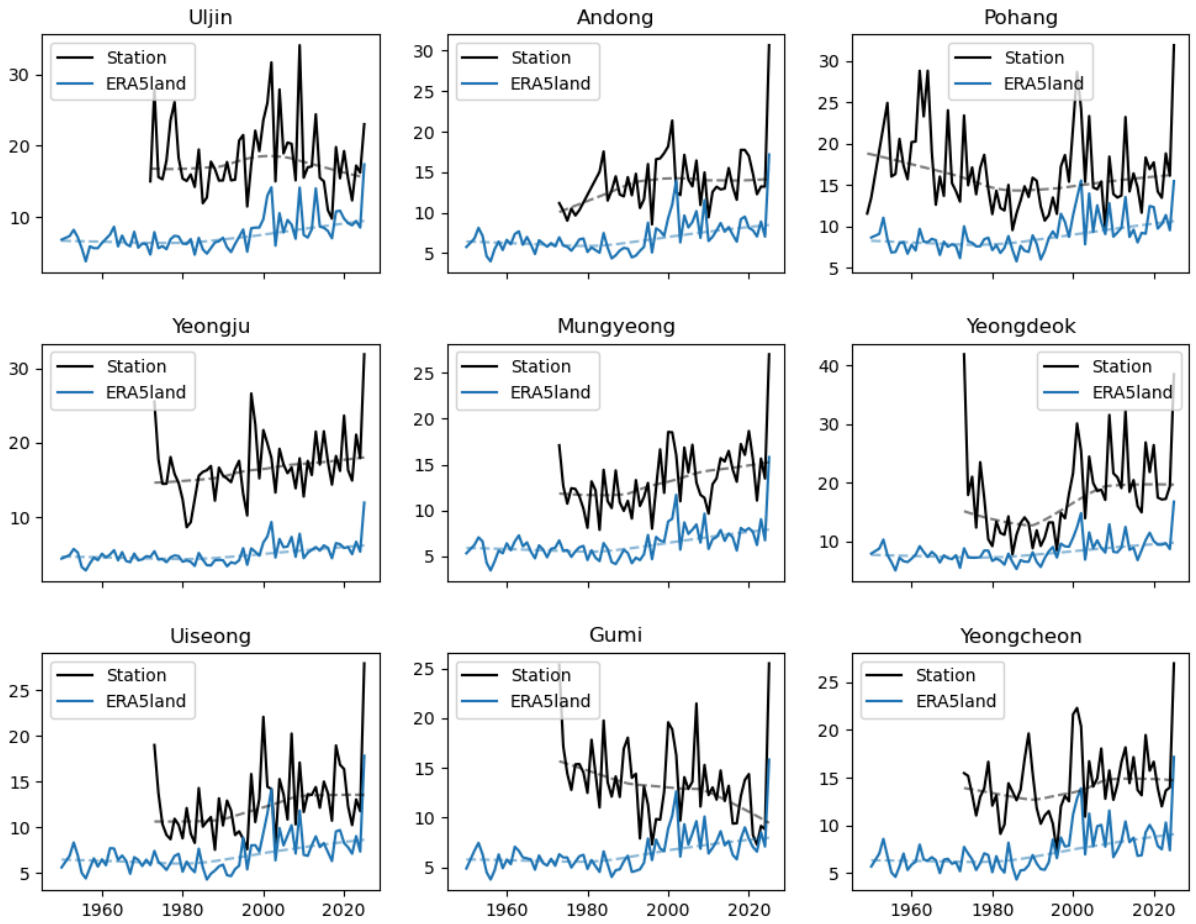

Figure 3.4: *Time series of HDWI5x at nine stations (black) and from the nearest grid cell in ERA5-land (blue). Dashed lines represent a nonparametric loess smoother showing the trend over time.*

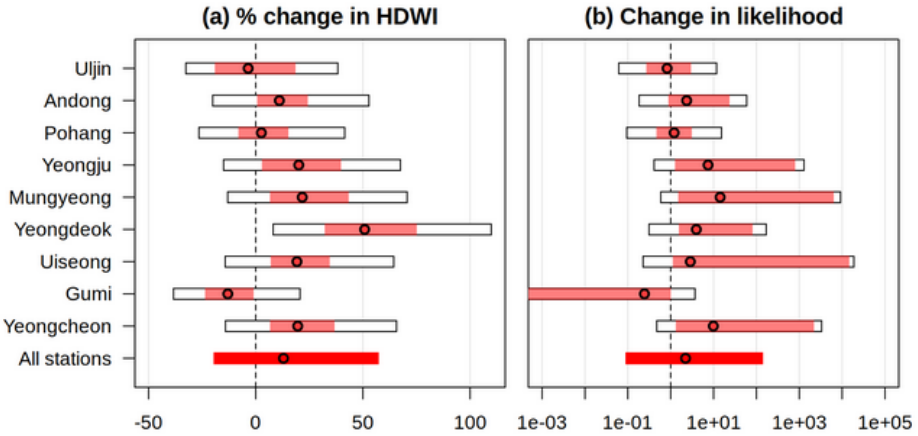

Figure 3.5: *Estimated change in* ***(a)*** *March HDWI5x and* ***(b)*** *likelihood of a similarly extreme March HDWI5x event in each station (light red bars) and precision-weighted average over all nine stations (dark red bar). For a more detailed explanation of the weighting algorithm, see Section 6.*

3.2 Trends in precipitation

3.2.1 Trends in gridded reanalysis products

Figure 3.6 shows the log of February-March precipitation in the ERA5-land dataset, as a function of time (panel a) and of GMST (panel b); corresponding figures for the raw precipitation data can be found in Figure A3.2. The nonparametric smoothed trend (dashed green line) is fairly linear in GMST, suggesting that the mean trend is relatively well represented by the linear model. In the return level plots (panel c) most of the points representing the observed HDWI5x values lie close to the line representing the expected values, indicating that the model fits the data well.

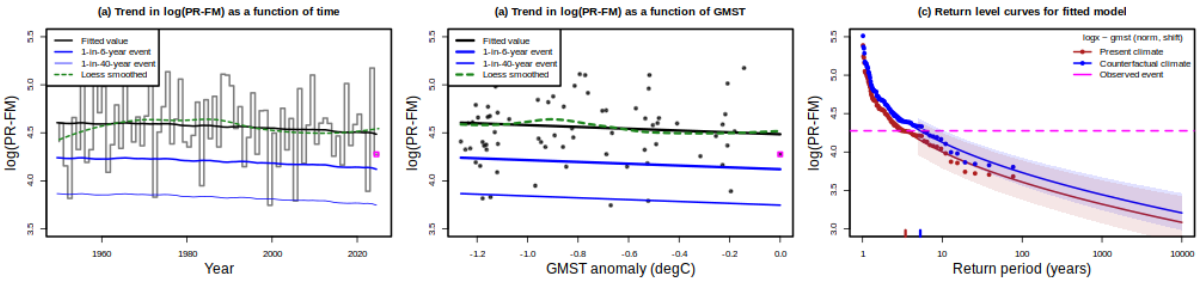

Figure 3.6: *February-March precipitation and fitted linear trends (ERA5-land).* ***(a)*** *Fitted trend in PR-FM over time; the heavy black line indicates the location of the distribution; blue lines indicate the 6-year and 40-year expected return level; green dashed line is a nonparametric Loess smoother and the pink dot shows the total rainfall in February-March 2025.* ***(b)*** *as (a), but showing PR-FM as a function of GMST anomaly with respect to 2025.* ***(c)*** *Expected return levels of PR-FM over the study region in the 2025 climate (red lines) and in a 1.3C cooler counterfactual climate (blue line), estimated from the statistical model. Shaded regions represent 95% confidence intervals obtained via a bootstrapping procedure. The pink line shows the rainfall during February-March 2025. Red and blue ticks at the x axis indicate the estimated return level of February-March 2025 in the 2025 climate and counterfactual climate.*

February-March 2025 was relatively dry over South Korea, but not particularly unusual; in the current climate, similarly dry periods are expected to occur around once every 3-4 years (95% confidence interval: 2 - 8 years), implying that there is roughly a 30% chance of February-March being as dry as 2025 in South Korea. For the attribution analysis we use a return period of 5 years, to evaluate changes in moderately dry periods.

According to the statistical model, mean February-March rainfall across South Korea has decreased slightly in the ERA5-land dataset, and is now an estimated 11% lower than in a 1.3C cooler climate, although the uncertainty around this trend is high (95% confidence interval: -33% to +21%); similarly dry periods are now around 50% more likely (95% confidence interval: 50% less likely to 3.8 times more likely). These results are summarised in Table 3.2.

Dataset	Event magnitude (mm)	Return period	Change in log(PR-FM)	% Change in PR-FM	Probability ratio
ERA5-land	72	3.45 (2.03 - 8.28)	-0.12 (-0.40 - 0.19)	-11.6 (-33.17 - 21.07)	1.53 (0.48 - 3.88)

Table 3.3: *Summary of fitted model results for February-March precipitation. Recorded value; return period of 2025 PR-FM in the 2025 climate; probability ratio, absolute change in log(PR-FM) and % change in PR-FM associated with 1.3°C of global warming. Figures in parenthesis indicate 95% confidence interval obtained via bootstrapping. Statistically significant changes are highlighted in* ***bold****.*

3.2.2 Trends in station data

We again evaluate the trends in ERA5-land against observations from nine stations in the most impacted area. Time series of February-March precipitation at each station and the closest grid cell are shown in Figure 3.7. In all stations, ERA5-land captures the local rainfall totals well from around 2000 onwards; however, in many of the stations the totals from 1973-2000 are somewhat lower than those in ERA5-land, leading to an apparent increasing trend. The station records contain many dates with no observation, and it is not clear whether these indicate an observation of zero rainfall or missing data; to test this, we compared the mean February-March rainfall rate on days for which precipitation was recorded at each station (Figure A3.3). Here, ERA5-land replicates the rainfall rates more closely; we therefore do not evaluate trends in rainfall at the individual stations, but are confident that ERA5-land is performing well in this region.

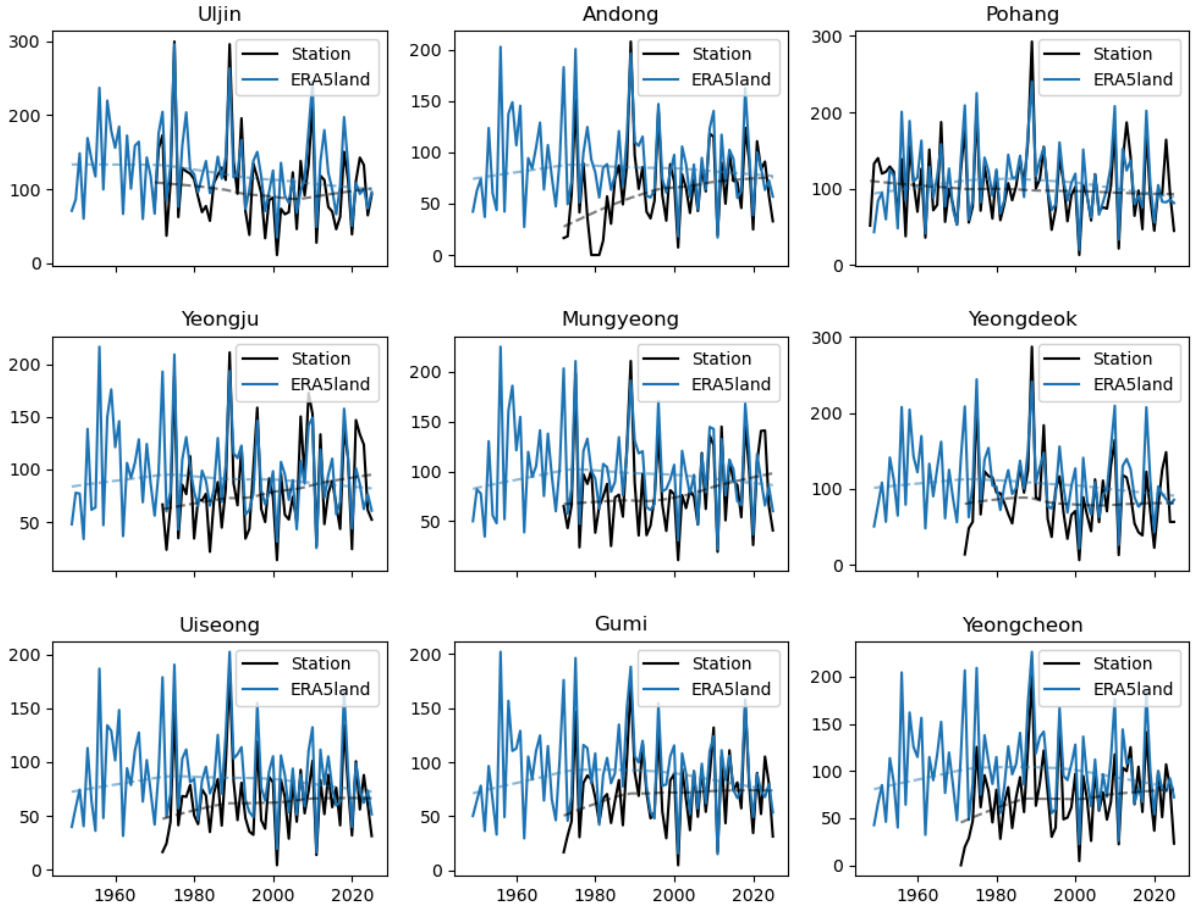

Figure 3.7: *Time series of PR-FM (mm) at nine stations (black) and from the nearest grid cell in ERA5-land (blue). Dashed lines represent a nonparametric loess smoother showing the trend over time.*

4 Model evaluation

The climate models are evaluated against ERA5-land for their ability to capture the seasonal cycle of mean daily HDWI, maximum temperature and rainfall over South Korea. Models are considered 'good' if they recreate the full seasonal cycle; 'reasonable' if they replicate spring trends faithfully; and 'bad' if the spring cycle is not well represented. Spatial patterns are not assessed because the resolution of the models used is typically too coarse to replicate them.

The models are then evaluated on how closely the parameters of the fitted statistical model (for a normal distribution, the standard deviation; for a GEV, both the scale and shape parameters) match those estimated using the observational dataset. In many of the models, HDWI was overdispersed compared to ERA5-land (meaning that the models have higher scale parameters) but the shape parameter was well estimated, so the overall decision to include or exclude the model was based primarily on the shape parameter and seasonal cycle.

The models are labelled as 'good' if the best estimate of each parameter falls within the bounds estimated from the observations; 'reasonable' if the confidence interval for the model overlaps with the range estimated from the observations; or 'bad' if the ranges do not overlap. If the model is 'good' for all criteria, we give it an overall rating of 'good'. We rate the model as 'reasonable' or 'bad', if it is rated 'reasonable' or 'bad', respectively, for at least one criterion. Where multiple versions of the same model passed evaluation, we retained the highest-resolution version.

Tables 4.1, 4.2 and 4.3 below we show the results of the model validation for HDWI5x, TX5x and PR-FM over South Korea. All models deemed 'good' or 'reasonable' were included in the final analysis. Plots comparing the seasonal cycle for each model with ERA5-land can be found in Figures A4.1-A4.3 (for HDWI) and A4.4-A4.6 (for precipitation). All models replicated the seasonal cycle of temperature comparably well, so are not shown.

Table 4.1: *Evaluation of the climate models considered for attribution of March HDWI5x over South Korea. For each model, the best estimate of the scale and shape parameters is shown, along with a 95% confidence obtained via bootstrapping. The overall evaluation is shown in the right-hand column.*

Observations / models	**Years**	**SC**	**Scale**	**Shape**	**Include?**
ERA5-land	1950 - 2025		0.81 (0.66, 0.95)	-0.02 (-0.22, 0.15)	
AWI-CM3					
cmip6_CanESM5_r1i1p1f1	1852 - 2099	Reasonable	1.44 (1.2, 1.66)	-0.23 (-0.38, -0.09)	Y

cmip6_CMCC-ESM2_r1i1p1f1	1852 - 2064	Reasonable	1.01 (0.8, 1.15)	-0.11 (-0.26, 0.13)	Y
cmip6_CNRM-CM6-1_r1i1p1f2	1852 - 2099	Reasonable	1.28 (1.03, 1.48)	-0.01 (-0.15, 0.18)	Y
cmip6_EC-Earth3-CC_r1i1p1f1	1852 - 2050	Reasonable	1.13 (0.9, 1.27)	-0.15 (-0.32, 0.06)	Y
cmip6_EC-Earth3-Veg-LR_r1i1p1f1	1979 - 2050	Reasonable	1.11 (0.8, 1.36)	-0.26 (-0.55, 0)	Y
cmip6_GFDL-CM4_r1i1p1f1	1990 - 2054	Bad	0.97 (0.62, 1.17)	-0.18 (-0.67, 0.34)	N
cmip6_INM-CM4-8_r1i1p1f1	1852 - 2064	Reasonable	1.38 (1.06, 1.63)	-0.08 (-0.3, 0.12)	Y
cmip6_INM-CM5-0_r1i1p1f1	1852 - 2064	Reasonable	1.45 (1.26, 1.65)	-0.32 (-0.57, -0.21)	Y
cmip6_IPSL-CM6A-LR_r1i1p1f1	1852 - 2099	Good	1.45 (1.19, 1.73)	0.07 (-0.08, 0.26)	Y
cmip6_KACE-1-0-G_r1i1p1f1	1853 - 2100	Bad	1.92 (1.49, 2.25)	-0.13 (-0.25, 0.08)	N
cmip6_MIROC6_r1i1p1f1	1852 - 2054	Bad	1.08 (0.87, 1.28)	-0.08 (-0.35, 0.1)	N
cmip6_MPI-ESM1-2-LR_r1i1p1f1	1852 - 2054	Bad	2.57 (2.11, 2.97)	-0.04 (-0.18, 0.14)	N
cmip6_MRI-ESM2-0_r1i1p1f1	2000 - 2064	Good	0.87 (0.24, 1.15)	0.12 (-0.46, 1.91)	N
highressst_CNRM-CM6-1_r1i1p1f2	1950 - 2050	Reasonable	2.52 (2.07, 2.88)	-0.1 (-0.31, 0.06)	Y
highressst_CNRM-CM6-1-HR_r1i1p1f2	1950 - 2050	Reasonable	2.05 (1.57, 2.45)	-0.27 (-0.61, 0.01)	N
highressst_EC-Earth3P_r1i1p1f1	1950 - 2049	Reasonable	2.18 (1.75, 2.54)	-0.03 (-0.18, 0.15)	N

highressst_EC-Earth3P-HR_r1i1p1f1	1950 - 2049	Reasonable	1.86 (1.55, 2.22)	-0.15 (-0.48, 0.04)	Y
highressst_HadGEM3-GC31-HM_r1i1p1f1	1950 - 2050	Reasonable	1.79 (1.17, 2.17)	0 (-0.14, 0.38)	Y
highressst_HadGEM3-GC31-LM_r1i14p1f1	1950 - 2050	Reasonable	2.26 (1.71, 2.67)	-0.16 (-0.49, 0.05)	N
highressst_HadGEM3-GC31-MM_r1i1p1f1	1950 - 2050	Reasonable	1.94 (1.58, 2.25)	-0.18 (-0.32, -0.04)	N
AM2.5C360_06	1871-2100		1.98 (1.61, 2.32)	0.06 (-0.1, 0.24)	Y
AM2.5C360_07	1871-2100		2.27 (1.88, 2.61)	-0.08 (-0.31, 0.12)	Y
AM2.5C360_08	1871-2100		2.16 (1.84, 2.43)	-0.1 (-0.24, 0.02)	Y
FLOR_01	1860-2100		1.51 (1.17, 1.85)	0.25 (0.02, 0.5)	Y
FLOR_02	1860-2100		1.43 (1.17, 1.64)	-0.06 (-0.27, 0.1)	Y
FLOR_03	1860-2100		1.49 (1.17, 1.79)	0.14 (-0.1, 0.39)	Y
FLOR_04	1860-2100		1.46 (1.16, 1.71)	0.13 (-0.01, 0.31)	Y
FLOR_05	1860-2100		1.33 (1.08, 1.58)	0.15 (-0.01, 0.31)	Y
FLOR_06	1860-2100		1.29 (0.97, 1.57)	0.24 (0.01, 0.5)	Y
FLOR_07	1860-2100		1.39 (1.13, 1.63)	0.07 (-0.08, 0.25)	Y
FLOR_08	1860-2100		1.52 (1.11, 1.8)	0.07 (-0.11, 0.38)	Y
FLOR_09	1860-2100		1.29 (1.01, 1.55)	0.17 (-0.02, 0.39)	Y

FLOR_10	1860-2100		1.53 (1.23, 1.79)	0.09 (-0.08, 0.29)	Y

Table 4.2: *Evaluation of the climate models considered for attribution of March TX5x over South Korea. For each model, the best estimate of the scale and shape parameters is shown, along with a 95% confidence obtained via bootstrapping. The overall evaluation is shown in the right-hand column.*

Observations / models	**Scale**	**Shape**	**Include?**
ERA5Land	1.72 (1.36, 2.04)	-0.24 (-0.42, -0.06)	
AWI-CM3-25km	1.72 (1.41, 1.98)	-0.38 (-0.65, -0.27)	Y
cmip6_ACCESS-CM2_r1i1p1f1	1.21 (0.91, 1.4)	-0.25 (-0.4, 0.02)	N
cmip6_ACCESS-ESM1-5_r1i1p1f1	1.05 (0.85, 1.19)	-0.16 (-0.37, -0.02)	N
cmip6_AWI-CM-1-1-MR_r1i1p1f1	2.36 (1.85, 2.78)	-0.22 (-0.32, -0.08)	N
cmip6_BCC-CSM2-MR_r1i1p1f1	2.3 (1.79, 2.69)	-0.35 (-0.59, -0.18)	N
cmip6_CanESM5_r1i1p1f1	1.66 (1.41, 1.88)	-0.3 (-0.54, -0.19)	Y
cmip6_CMCC-ESM2_r1i1p1f1	2.24 (1.75, 2.61)	-0.34 (-0.51, -0.19)	N
cmip6_CNRM-CM6-1_r1i1p1f2	1.91 (1.52, 2.22)	-0.23 (-0.41, -0.1)	Y
cmip6_EC-Earth3_r1i1p1f1	1.93 (1.62, 2.22)	-0.32 (-0.52, -0.2)	Y
cmip6_EC-Earth3-CC_r1i1p1f1	1.61 (1.34, 1.85)	-0.26 (-0.47, -0.06)	Y
cmip6_EC-Earth3-Veg_r1i1p1f1	1.82 (1.52, 2.09)	-0.42 (-0.6, -0.3)	Y
cmip6_EC-Earth3-Veg-LR_r1i1p1f1	1.49 (1.26, 1.66)	-0.12 (-0.38, 0.02)	Y
cmip6_FGOALS-g3_r1i1p1f1	2 (1.55, 2.37)	-0.38 (-0.6, -0.25)	Y
cmip6_GFDL-CM4_r1i1p1f1	1.53 (1.27, 1.73)	-0.16 (-0.45, -0.04)	Y
cmip6_GFDL-ESM4_r1i1p1f1	1.6 (1.33, 1.82)	-0.18 (-0.36, 0.03)	Y

cmip6_HadGEM3-GC31-LL_r1i1p1f3	1.61 (1.35, 1.84)	-0.3 (-0.48, -0.2)	Y
cmip6_INM-CM4-8_r1i1p1f1	1.61 (1.19, 1.92)	-0.32 (-0.47, -0.12)	Y
cmip6_INM-CM5-0_r1i1p1f1	1.74 (1.49, 1.94)	-0.37 (-0.52, -0.22)	Y
cmip6_IPSL-CM6A-LR_r1i1p1f1	2.63 (2.21, 2.98)	-0.13 (-0.33, -0.02)	N
cmip6_KACE-1-0-G_r1i1p1f1	1.8 (1.46, 2.08)	-0.21 (-0.36, -0.07)	Y
cmip6_KIOST-ESM_r1i1p1f1	2.45 (2.08, 2.81)	-0.24 (-0.46, -0.08)	N
cmip6_MIROC-ES2L_r1i1p1f2	1.42 (1.13, 1.69)	-0.45 (-0.68, -0.24)	N
cmip6_MIROC6_r1i1p1f1	1.41 (1.14, 1.63)	-0.28 (-0.43, -0.15)	Y
cmip6_MPI-ESM1-2-LR_r1i1p1f1	1.84 (1.51, 2.16)	-0.2 (-0.44, -0.04)	Y
cmip6_MRI-ESM2-0_r1i1p1f1	2.02 (1.71, 2.31)	-0.38 (-0.55, -0.24)	Y
cmip6_NESM3_r1i1p1f1	1.79 (1.52, 2.04)	-0.23 (-0.46, -0.09)	Y
cmip6_NorESM2-LM_r1i1p1f1	2.37 (1.91, 2.73)	-0.55 (-0.78, -0.38)	N
cmip6_NorESM2-MM_r1i1p1f1	1.91 (1.61, 2.19)	-0.43 (-0.61, -0.31)	N
cmip6_TaiESM1_r1i1p1f1	1.81 (1.42, 2.15)	-0.28 (-0.52, 0.03)	Y
cmip6_UKESM1-0-LL_r1i1p1f2	1.56 (1.31, 1.78)	-0.22 (-0.46, -0.12)	Y
highressst_CNRM-CM6-1_r1i1p1f2	1.72 (1.41, 1.95)	-0.2 (-0.49, -0.08)	Y
highressst_CNRM-CM6-1-HR_r1i1p1f2	1.98 (1.6, 2.28)	-0.2 (-0.43, -0.05)	Y
highressst_EC-Earth3P_r1i1p1f1	1.3 (1.03, 1.51)	-0.17 (-0.32, -0.01)	N
highressst_EC-Earth3P-HR_r1i1p1f1	1.47 (1.11, 1.74)	-0.19 (-0.32, 0)	Y
highressst_HadGEM3-GC31-HM_r1i1p1f1	2.11 (1.69, 2.45)	-0.26 (-0.41, -0.1)	N

highressst_HadGEM3-GC31-LM_r1i14p1f1	1.66 (1.34, 1.99)	-0.32 (-0.57, -0.09)	Y
highressst_HadGEM3-GC31-MM_r1i1p1f1	2.08 (1.69, 2.4)	-0.17 (-0.4, -0.03)	N

Table 4.3: *Evaluation of the climate models considered for attribution of PR-FM over South Korea. For each model, the best estimate of the scale and shape parameters is shown, along with a 95% confidence obtained via bootstrapping. The overall evaluation is shown in the right-hand column.*

Observations / models	**SC**	**Shape**	**Include?**
ERA5-land		0.38 (0.31, 0.43)	
AWI-CM3-25km	good	0.36 (0.3, 0.41)	Y
cmip6_ACCESS-ESM1-5_r1i1p1f1	good	0.4 (0.34, 0.44)	Y
cmip6_CanESM5_r1i1p1f1	bad	0.44 (0.37, 0.5)	N
cmip6_CESM2-WACCM_r1i1p1f1	reasonable	0.52 (0.44, 0.58)	N
cmip6_CMCC-CM2-SR5_r1i1p1f1	reasonable	0.41 (0.34, 0.46)	Y
cmip6_CMCC-ESM2_r1i1p1f1	reasonable	0.57 (0.49, 0.64)	N
cmip6_CNRM-CM6-1_r1i1p1f2	good	0.45 (0.34, 0.55)	Y
cmip6_EC-Earth3_r1i1p1f1	good	0.42 (0.35, 0.48)	Y
cmip6_EC-Earth3-CC_r1i1p1f1	good	0.38 (0.31, 0.44)	n
cmip6_EC-Earth3-Veg_r1i1p1f1	good	0.38 (0.33, 0.42)	n
cmip6_EC-Earth3-Veg-LR_r1i1p1f1	good	0.42 (0.36, 0.47)	n
cmip6_FGOALS-g3_r1i1p1f1	good	0.43 (0.35, 0.49)	Y
cmip6_GFDL-CM4_r1i1p1f1	good	0.44 (0.36, 0.5)	Y
cmip6_GFDL-ESM4_r1i1p1f1	good	0.37 (0.29, 0.43)	Y
cmip6_HadGEM3-GC31-LL_r1i1p1f3	reasonable	0.45 (0.38, 0.52)	Y
cmip6_INM-CM4-8_r1i1p1f1	bad	0.29 (0.24, 0.33)	N
cmip6_INM-CM5-0_r1i1p1f1	bad	0.36 (0.31, 0.4)	N

cmip6_IPSL-CM6A-LR_r1i1p1f1	reasonable	0.44 (0.37, 0.5)	Y
cmip6_KACE-1-0-G_r1i1p1f1	reasonable	0.44 (0.37, 0.5)	Y
cmip6_KIOST-ESM_r1i1p1f1	bad	0.38 (0.32, 0.44)	N
cmip6_MIROC-ES2L_r1i1p1f2	bad	0.47 (0.39, 0.54)	N
cmip6_MIROC6_r1i1p1f1	bad	0.43 (0.37, 0.48)	N
cmip6_MPI-ESM1-2-LR_r1i1p1f1	good	0.41 (0.34, 0.47)	Y
cmip6_MRI-ESM2-0_r1i1p1f1	good	0.5 (0.39, 0.61)	Y
cmip6_NESM3_r1i1p1f1	bad	0.32 (0.26, 0.37)	N
cmip6_NorESM2-LM_r1i1p1f1	reasonable	0.5 (0.4, 0.58)	n
cmip6_NorESM2-MM_r1i1p1f1	reasonable	0.43 (0.37, 0.49)	Y
cmip6_TaiESM1_r1i1p1f1	good	0.57 (0.42, 0.72)	Y
cmip6_UKESM1-0-LL_r1i1p1f2	good	0.47 (0.39, 0.53)	Y
highressst_CNRM-CM6-1_r1i1p1f2	reasonable	0.44 (0.37, 0.49)	n
highressst_CNRM-CM6-1-HR_r1i1p1f2	reasonable	0.33 (0.27, 0.37)	Y
highressst_EC-Earth3P_r1i1p1f1	good	0.38 (0.31, 0.43)	n
highressst_EC-Earth3P-HR_r1i1p1f1	good	0.41 (0.35, 0.45)	Y
highressst_HadGEM3-GC31-HM_r1i1p1f1	reasonable	0.42 (0.33, 0.49)	Y
highressst_HadGEM3-GC31-LM_r1i14p1f1	bad	0.4 (0.33, 0.47)	N
highressst_HadGEM3-GC31-MM_r1i1p1f1	reasonable	0.4 (0.33, 0.46)	N

5 Multi-method multi-model attribution

Tables 5.1-5.3 show probability ratios (PR) and changes in intensity (ΔI) in each index, for ERA5-land and for those models that passed the evaluation described in Section 4. These changes are synthesised into a single overarching attribution result in Section 6.

Table 5.1: *Probability ratio and change in intensity for 100-year HDWI5x over South Korea, for ERA5-land and each model that passed evaluation: (a) from the preindustrial climate to the present and (b) from the present to 2.6°C above preindustrial.*

	(a) -1.3C vs present		(b) Present vs +1.3C	
Observations / models	**Probability ratio**	**Change in intensity (%)**	**Probability ratio**	**Change in intensity (%)**
ERA5-land	13.72 (3.33, inf)	25.6 (16.0, 37.6)		
cmip6_CanESM5_r1i1p1f1	5.35 (1.89, 82.12)	8.47 (3.94, 13.91)	1.96 (1.52, 2.85)	4.4 (3.27, 5.81)
cmip6_CMCC-ESM2_r1i1p1f1	2.3 (1.07, 8.95)	6.02 (0.62, 11.65)	3.64 (2.13, 6.78)	7.85 (5.87, 9.95)
cmip6_CNRM-CM6-1_r1i1p1f2	1.47 (0.8, 3.78)	2.7 (-1.59, 7.66)	2.04 (1.47, 3.24)	5 (3.17, 6.76)
cmip6_EC-Earth3-CC_r1i1p1f1	2.86 (1.22, 9.43)	5.85 (1.32, 10.51)	2.12 (1.4, 3.33)	5 (2.46, 7.37)
cmip6_EC-Earth3-Veg-LR_r1i1p1f1	#VALUE!	8.4 (-7.78, 23.85)	3.43 (1.18, 10.86)	5.59 (0.7, 9.86)
cmip6_INM-CM4-8_r1i1p1f1	0.47 (0.17, 1.02)	-4.98 (-10.39, 0.2)	1.39 (0.99, 2.07)	2.12 (-0.06, 4.23)
cmip6_INM-CM5-0_r1i1p1f1	1.36 (0.29, 43.37)	1.28 (-6.1, 8.89)	2.9 (1.68, 5.2)	4.71 (2.26, 6.82)
cmip6_IPSL-CM6A-LR_r1i1p1f1	1.21 (1.02, 1.73)	4.18 (0.55, 9.71)	1.32 (1.18, 1.65)	5.45 (4.14, 7.29)
highressst_CNRM-CM6-1_r1i1p1f2	1.11 (0.27, 417.02)	0.64 (-8.36, 13.17)	3.01 (1.43, 10.28)	5.59 (2.14, 9.55)
highressst_EC-Earth3P-HR_r1i1p1f1	#VALUE!	0.29 (-9.1, 9.69)	4.05 (1.99, 12.68)	6.67 (3.41, 9.95)
highressst_HadGEM3-GC31-HM_r1i1p1f1	2 (0.8, 10.56)	6.41 (-1.94, 16.21)	1.82 (1.03, 4.63)	5.14 (0.63, 9.87)

AM2.5C360_06	1.07 (0.61, 2.29)	0.95 (-7.04, 11.52)	1.1 (0.8, 1.75)	1.22 (-3.56, 5.85)
AM2.5C360_07	1.33 (0.61, 4.67)	3.7 (-6.06, 16.39)	1.63 (1.11, 2.74)	5.94 (1.39, 10.48)
AM2.5C360_08	1.68 (0.52, 4.44)	5.57 (-4.91, 15.47)	1.64 (0.98, 2.68)	5.14 (-0.25, 9.87)
FLOR_01	1.05 (0.82, 1.48)	1.01 (-3.64, 6.95)	1.2 (0.99, 1.8)	3.01 (-0.15, 7.2)
FLOR_02	1.63 (0.84, 6.27)	5.28 (-1.92, 14.06)	2.03 (1.35, 3.94)	7.49 (4.06, 11.07)
FLOR_03	1.3 (1.1, 2.06)	6.8 (3.02, 13.09)	1.36 (1.16, 1.78)	5.91 (3.77, 8.53)
FLOR_04	1.45 (1.07, 2.52)	7.41 (1.64, 15.48)	1.36 (1.09, 1.91)	4.87 (1.76, 8.09)
FLOR_05	1.24 (0.95, 1.92)	3.79 (-1, 10.05)	1.46 (1.21, 2.08)	5.99 (3.62, 8.72)
FLOR_06	1.08 (0.86, 1.41)	1.61 (-2.49, 6.43)	1.23 (1.06, 1.73)	3.88 (1.32, 7.27)
FLOR_07	1.81 (1.24, 3.64)	9.57 (3.97, 16.99)	1.76 (1.2, 3.39)	6.65 (2.82, 10.56)
FLOR_08	1.04 (0.75, 1.72)	0.75 (-5.32, 7.76)	1.51 (1.17, 2.25)	6.12 (3.19, 8.95)
FLOR_09	1.76 (1.26, 3.49)	10.33 (4.61, 17.6)	1.48 (1.22, 2.21)	6.48 (4.04, 9.8)
FLOR_10	1.68 (1.17, 4.14)	7.88 (2.9, 15.24)	1.38 (1.12, 1.95)	4.89 (2.06, 7.9)

Table 5.2: *Probability ratio and change in intensity for 100-year TX5x over South Korea, for ERA5-land and each model that passed evaluation: (a) from the preindustrial climate to the present and (b) from the present to 2.6°C above preindustrial.*

Model / Observations	**Threshold for return period 10 yr**	**Current warming level [˚C]**	**Probability ratio PR [-]**	**Change in intensity ΔI [˚C]**	**Future warming level [˚C]**	**Probability ratio PR [-]**	**Change in intensity ΔI [˚C]**
ERA5land	19.9 ˚C	1.2	∞ (12 ... ∞)	3.7 (1.8 ... 5.5)			
AWI-CM3-25km	17 ˚C	1.2	∞ (4.9e+5 ...	2.0 (1.1 ...	2.0	11 (5.2 ... 31)	1.6 (1.1 ...

()			∞)	2.9)			2.0)
cmip6_CanESM5_r1i1p1f1 ()	16 ˚C	1.2	5.5e+2 (8.0 ... ∞)	1.7 (0.98 ... 2.4)	2.0	8.0 (5.9 ... 13)	1.5 (1.3 ... 1.7)
cmip6_CNRM-CM6-1_r1i1p1f2 ()	17 ˚C	1.2	5.7 (1.1 ... 1.1e+3)	1.0 (0.074 ... 2.0)	2.0	4.6 (3.2 ... 7.4)	1.3 (0.93 ... 1.6)
cmip6_EC-Earth3_r1i1p1f1 ()	17 ˚C	1.2	7.3 (1.3 ... 1.2e+6)	0.76 (0.13 ... 1.4)	2.0	5.8 (3.4 ... 9.8)	1.2 (0.78 ... 1.5)
cmip6_EC-Earth3-CC_r1i1p1f1 ()	17 ˚C	1.2	6.9 (2.3 ... ∞)	1.0 (0.57 ... 1.6)	2.0	4.2 (2.4 ... 10)	1.1 (0.72 ... 1.6)
cmip6_EC-Earth3-Veg_r1i1p1f1 ()	17 ˚C	1.2	6.3 (1.4 ... ∞)	0.82 (0.19 ... 1.5)	2.0	5.6 (3.1 ... 16)	1.2 (0.81 ... 1.7)
cmip6_EC-Earth3-Veg-LR_r1i1p1f1 ()	16 ˚C	1.2	1.4 (0.39 ... 9.6)	0.24 (-0.62 ... 1.1)	2.0	3.9 (2.1 ... 8.1)	1.0 (0.57 ... 1.5)
cmip6_FGOALS-g3_r1i1p1f1 ()	17 ˚C	1.2	29 (2.0 ... ∞)	1.3 (0.34 ... 2.3)	2.0	5.1 (2.2 ... 14)	1.2 (0.56 ... 1.9)
cmip6_GFDL-CM4_r1i1p1f1 ()	17 ˚C	1.2	11 (1.2 ... ∞)	1.3 (0.15 ... 2.3)	2.0	4.4 (2.7 ... 8.4)	1.2 (0.82 ... 1.5)
cmip6_GFDL-ESM4_r1i1p1f1 ()	15 ˚C	1.2	3.8 (0.54 ... 4.2e+2)	0.67 (-0.35 ... 1.7)	2.0	4.4 (2.3 ... 8.7)	1.0 (0.49 ... 1.6)
cmip6_HadGEM3-GC31-LL_r1i1p1f3 ()	15 ˚C	1.2	2.2e+3 (3.3 ... ∞)	1.2 (0.37 ... 1.9)	2.0	13 (9.1 ... 21)	1.5 (1.3 ... 1.7)
cmip6_INM-CM4-8_r1i1p1f1 ()	18 ˚C	1.2	50 (0.62 ... ∞)	0.60 (-0.16 ... 1.3)	2.0	11 (6.8 ... 16)	1.1 (0.81 ... 1.4)
cmip6_INM-CM5-0_r1i1p1f1 ()	18 ˚C	1.2	4.2e+3 (3.3 ... ∞)	1.6 (0.50 ... 2.7)	2.0	8.7 (5.1 ... 19)	1.5 (1.1 ... 1.9)
cmip6_KACE-1-0-G_r1i1p1f1 ()	19 ˚C	1.2	28 (3.7 ... ∞)	1.4 (0.75 ... 2.1)	2.0	7.7 (4.9 ... 14)	1.8 (1.5 ... 2.0)
cmip6_MIROC6_r1i1p1f1 ()	19 ˚C	1.2	17 (1.4 ... ∞)	1.3 (0.17 ... 2.3)	2.0	6.7 (3.5 ... 18)	1.4 (0.85 ... 1.9)
cmip6_MPI-ESM1-2-LR_r1i1p1f1 ()	19 ˚C	1.2	4.5 (1.3 ... 1.9e+2)	1.2 (0.28 ... 2.2)	2.0	3.1 (1.7 ... 6.7)	1.0 (0.42 ... 1.7)
cmip6_MRI-ESM2-0_r1i1p1f1 ()	17 ˚C	1.2	8.3 (0.38 ... ∞)	0.66 (-0.49 ... 1.7)	2.0	6.0 (3.6 ... 9.8)	1.0 (0.69 ... 1.4)
cmip6_NESM3_r1i1p1f1 ()	13 ˚C	1.2	22 (1.0 ... ∞)	0.92 (0.00015 ... 1.6)	2.0	6.7 (4.5 ... 12)	1.2 (0.92 ... 1.4)
cmip6_TaiESM1_r1i1p1f1 ()	20 ˚C	1.2	31 (1.8 ... ∞)	1.3 (0.29 ... 2.3)	2.0	7.2 (3.8 ... 13)	1.5 (1.0 ... 1.9)
cmip6_UKESM1-0-LL_r1i1p1f2 ()	15 ˚C	1.2	2.7 (0.60 ... 1.0e+2)	0.46 (-0.24 ... 1.2)	2.0	7.1 (5.0 ... 13)	1.2 (0.99 ... 1.3)
highressst_CNRM-CM6-1_r1i1p1f2 ()	19 ˚C	1.2	26 (0.80 ... ∞)	1.6 (-0.21 ... 3.2)	2.0	4.7 (2.4 ... 20)	1.2 (0.67 ... 1.8)
highressst_CNRM-CM6-1-HR_r1i1p1f2 ()	19 ˚C	1.2	2.9 (0.26 ... ∞)	0.75 (-1.5 ... 3.6)	2.0	6.3 (2.6 ... 21)	1.6 (0.79 ... 2.4)
highressst_EC-Earth3P-HR_r1i1p1f1 ()	18 ˚C	1.2	8.2 (0.75 ... ∞)	1.1 (-0.19 ... 2.5)	2.0	4.3 (1.4 ... 13)	1.1 (0.24 ... 2.1)

highressst_HadGEM3-GC31-LM_r1i14p1f1 ()	16 ˚C	1.2	1.2e+4 (0.24 ... ∞)	1.1 (-0.69 ... 2.9)	2.0	8.6 (3.3 ... 18)	1.1 (0.41 ... 1.8)

Table 5.3: *Probability ratio and change in intensity for 5-year PR-FM over South Korea, for ERA5-land and each model that passed evaluation: (a) from the preindustrial climate to the present and (b) from the present to 2.6°C above preindustrial.*

Model / Observations	**Threshold for return period 10 yr**	**Current warming level [˚C]**	**Probability ratio PR [-]**	**Change in intensity ΔI [mm/day]**	**Future warming level [˚C]**	**Probability ratio PR [-]**	**Change in intensity ΔI [%]**
ERA5land	4.276412406278 15 mm/day	1.2	1.5 (0.48 ... 3.9)	-12 (-33 ... 21)			
AWI-CM3-25km ()	3.2 mm/day	1.2	0.61 (0.36 ... 1.3)	15 (-5.6 ... 40)	2.0	0.80 (0.59 ... 1.0)	6.0 (-1.3 ... 12)
cmip6_ACCESS-ESM1-5_r1i1p1f1 ()	4.0 mm/day	1.2	1.6 (0.71 ... 4.9)	-12 (-32 ... 12)	2.0	0.64 (0.45 ... 0.89)	12 (3.6 ... 19)
cmip6_CMCC-CM2-SR5_r1i1p1f1 ()	4.2 mm/day	1.2	0.97 (0.57 ... 2.0)	1.0 (-18 ... 23)	2.0	0.78 (0.57 ... 1.0)	7.2 (-0.017 ... 15)
cmip6_CNRM-CM6-1_r1i1p1f2 ()	4.1 mm/day	1.2	2.2 (0.90 ... 6.8)	-18 (-38 ... 3.2)	2.0	0.86 (0.67 ... 1.1)	4.6 (-2.0 ... 11)
cmip6_EC-Earth3_r1i1p1f1 ()	4.3 mm/day	1.2	1.2 (0.68 ... 2.6)	-4.0 (-20 ... 12)	2.0	0.73 (0.53 ... 0.99)	7.6 (0.20 ... 14)
cmip6_FGOALS-g3_r1i1p1f1 ()	3.9 mm/day	1.2	1.1 (0.64 ... 2.4)	-3.6 (-19 ... 15)	2.0	0.83 (0.50 ... 1.2)	5.1 (-6.7 ... 16)
cmip6_GFDL-CM4_r1i1p1f1 ()	4.1 mm/day	1.2	1.4 (0.67 ... 3.8)	-9.3 (-29 ... 16)	2.0	0.70 (0.49 ... 0.96)	9.9 (1.1 ... 18)
cmip6_GFDL-ESM4_r1i1p1f1 ()	4.5 mm/day	1.2	0.59 (0.33 ... 1.6)	18 (-11 ... 52)	2.0	0.66 (0.34 ... 1.2)	10 (-4.1 ... 21)
cmip6_HadGEM3-GC31-LL_r1i1p1f3 ()	4.6 mm/day	1.2	0.69 (0.43 ... 1.4)	13 (-8.8 ... 39)	2.0	0.69 (0.56 ... 0.84)	9.9 (4.9 ... 15)
cmip6_IPSL-CM6A-LR_r1i1p1f1 ()	4.5 mm/day	1.2	1.5 (0.82 ... 3.2)	-9.7 (-24 ... 6.1)	2.0	0.85 (0.66 ... 1.1)	4.7 (-2.1 ... 10)
cmip6_KACE-1-0-G_r1i1p1f1 ()	4.5 mm/day	1.2	0.79 (0.49 ... 1.4)	8.0 (-8.8 ... 31)	2.0	0.79 (0.62 ... 0.99)	6.7 (0.40 ... 12)
cmip6_MPI-ESM1-2-LR_r1i1p1f1 ()	4.6 mm/day	1.2	0.86 (0.54 ... 1.9)	4.7 (-15 ... 24)	2.0	0.90 (0.57 ... 1.4)	2.9 (-13 ... 14)
cmip6_MRI-ESM2-0_r1i1p1	3.9 mm/day	1.2	3.3 (1.3 ... 14)	-29 (-47 ... -7.4)	2.0	0.82 (0.58 ... 1.2)	6.6 (-5.8 ... 16)

f1 ()							
cmip6_NorESM2-MM_r1i1p1f1 ()	4.5 mm/day	1.2	0.37 (0.25 ... 0.63)	56 (18 ... 1.1e+2)	2.0	0.58 (0.27 ... 1.0)	16 (-0.98 ... 30)
cmip6_TaiESM1_r1i1p1f1 ()	4.2 mm/day	1.2	0.56 (0.35 ... 1.0)	31 (-1.0 ... 79)	2.0	0.78 (0.58 ... 1.1)	9.0 (-2.0 ... 18)
cmip6_UKESM1-0-LL_r1i1p1f2 ()	4.4 mm/day	1.2	1.2 (0.61 ... 2.7)	-4.5 (-25 ... 19)	2.0	0.82 (0.61 ... 1.0)	7.0 (-1.7 ... 14)
highressst_CNRM-CM6-1-HR_r1i1p1f2 ()	4.6 mm/day	1.2	2.5 (0.60 ... 26)	-17 (-40 ... 14)	2.0	1.0 (0.54 ... 1.7)	-1.1 (-16 ... 12)
highressst_EC-Earth3P-HR_r1i1p1f1 ()	4.1 mm/day	1.2	3.9 (0.69 ... 48)	-27 (-51 ... 11)	2.0	1.0 (0.52 ... 1.8)	-0.061 (-20 ... 15)
highressst_HadGEM3-GC31-HM_r1i1p1f1 ()	4.8 mm/day	1.2	0.46 (0.27 ... 1.6)	33 (-11 ... 81)	2.0	0.71 (0.25 ... 1.4)	9.3 (-13 ... 27)

6 Hazard synthesis

For the 5-day maximum HDWI in March (HDWI5x), as well as the January to March rainfall (PR-FM) and the 5-day maximum temperatures in March (TX5x) over South Korea, we evaluate the influence of anthropogenic climate change by calculating the probability ratio as well as the change in intensity using observation-based products, in this case ERA5-land, and climate models. Models which do not pass the evaluation described in Section 5 are excluded from the analysis. The aim is to synthesise results from models that pass the evaluation along with the observations-based products, to give an overarching attribution statement.

Figures 6.1, 6.3 and 6.5 show the changes in probability and intensity for the observation-based product (blue) and models (red). Because there is only a single dataset in this case, the individual observation (light blue) and the summary bar for all observation-based products (dark blue) are identical. For the climate models, a term to account for intermodel spread is added in quadrature to the natural variability of the models. This is shown in the figures as white boxes around the light red bars. The dark red bar shows the model average, consisting of a weighted mean using the (uncorrelated) uncertainties due to natural variability. Single-model ensembles with multiple realisations (AM2.5 and FLOR) are first processed using the same algorithm, and the synthesised ensemble result is treated as a single model in the final synthesis.

Observation-based products and models are combined into a single result in two ways. Firstly, we neglect common model uncertainties beyond the intermodel spread, and compute the weighted average of models (dark red bar) and observations (dark blue bar): this is indicated by the magenta bar. Because, model uncertainty can be larger than the intermodel spread due to common model uncertainties, we also show the more conservative estimate of an unweighted, direct average of observations (dark blue bar) and models (dark red bar) contributing 50% each, indicated by the white box around the magenta bar in the synthesis figures.

To see whether the trends observed up to the present day continue in the future, we repeat the analysis for models only, comparing the three events as observed today with a 1.3C warmer climate. The results of these are shown in figures 6.2, 6.4 and 6.6.

In some instances, the trend is strong enough that the upper bound of the confidence interval round the probability ratio - and sometimes the central estimate - is infinite. In these instances, the infinite values are replaced with finite values inferred from other available information. If only the upper bound is missing, the difference between the central and lower values (a two-sigma interval, representing two standard deviations from the central estimate) is used to estimate the upper bound of a six-sigma interval; these rows are marked with *. If both the upper bound and central estimate are missing, the central estimate is first set to the maximum of the finite upper bounds, and then the upper bound is inferred as before; these rows are marked with **. In such cases the uncertainty intervals are so wide as to be essentially uninformative, but the inferred values allow the results to be more easily visualised.

For more detail on how the results are synthesised, see Otto et al. (2024).

6.1 HDWI5x

For the HDWI-based event definition we find that the best estimates of most climate models show an increase in the likelihood and intensity of the index, but the synthesised model result (dark red bar in figure 6.1) is lower than in the gridded observations described in Section 3.1. When combining the observations with models, based on the weighted average, we find an increase of about 13% in the intensity of the 5-day maximum March HDWI and roughly a doubling of the likelihood as the best estimates. While the uncertainties are comparably large, at least for the change in likelihood we do report the best estimates as our overarching results for the changes attributable to climate change, noting they might be conservative, but including a chance of a relatively large role of natural variability in the observed changes. The synthesised results are almost identical to the average of the available stations in the most affected area, which provide an additional line of evidence.

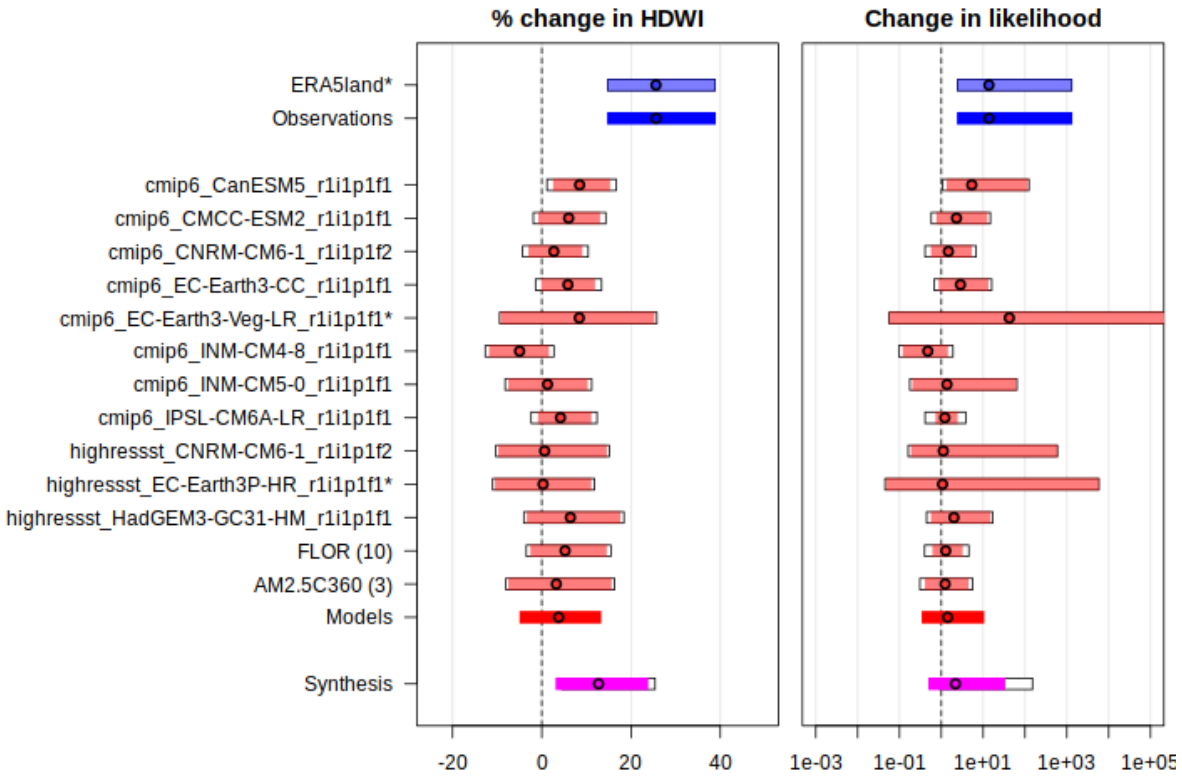

Figure 6.1: *Synthesis of (left) probability ratios and (right) relative intensity changes when comparing the return period and magnitudes of HDWI5x in South Korea between the current climate and a 1.3°C cooler climate.*

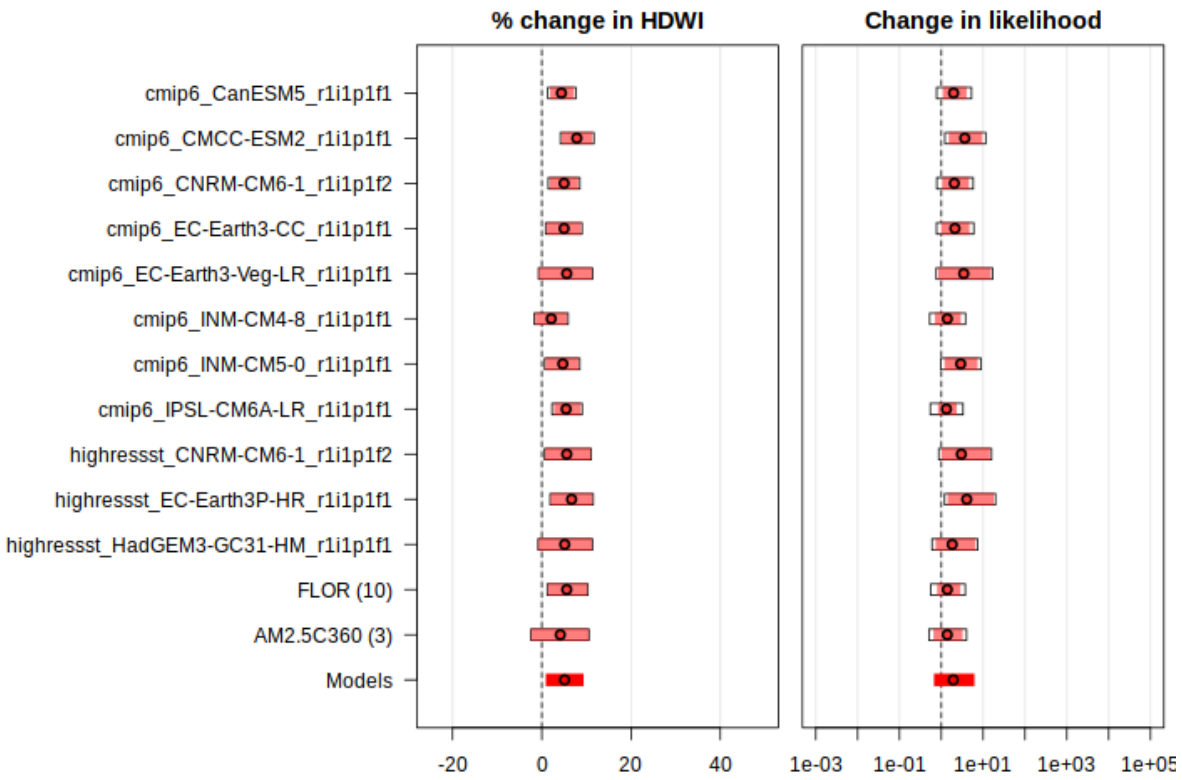

Figure 6.2: *As Figure 6.1, synthesising changes in HDWI5x between the current climate and a 1.3°C warmer climate (that is, a climate that is 2.6°C warmer than preindustrial).*

Source		Probability ratio (95% CI)	Intensity change (%) (95% CI)
Reanalysis	**Past- Present**	**13.7 (3.33, 957)**	**25.6 (16, 37.6)**
Models		1.41 (0.48, 7.51)	3.8 (-3.6, 11.9)
Synthesis		2.17 (0.69, 23.7)	**12.7 (4.5, 22.4)**
Models only	**Future**	1.93 (0.94, 4.36)	**5.1 (2.3, 8.0)**

Table 6.1: *Summary of synthesised changes in HDWI5x, presented in Figures 6.1 and 6.2. Statistically significant changes are highlighted in* ***bold****.*

The change in the HDWI5x event with future warming shows an increase in intensity and likelihood for all models, including those that show no change or a decrease for the changes up to now. This finding corroborates the attribution statement above and gives high confidence that human-induced climate change is the main driver of the increase in likelihood and intensity up till now.

6.2 TX5x

For the second event definition analysed, the 5-day maximum temperatures in March over South Korea (Figure 6.3 and 6.4), we find a very strong increase in the likelihood and intensity both when comparing today's climate with a 1.3°C cooler climate and when comparing a 1.3°C warmer future climate with the present. As with HDWI5x above, we find the increase in the observation-based product is much stronger (almost 4°C in intensity and infinite for the change in likelihood) than in the models, which show a synthesised increase in intensity that is about the global average of 1.3°C. Many of the models simulate infinite upper bounds for the confidence interval of the change in likelihood from past to present climate, and the overall synthesised probability ratio is more than 20; under a further 1.3°C of warming the probability ratio, which is estimated using longer time series including both historic and future warming and so has substantially lower uncertainty, is estimated to be around 7, and at least 3.

These findings, together with the analysis of the components of the HDWI in the observations (Section 3.1.2) suggest, that the trend in HDWI5x is primarily driven by the strong increase in temperature, but that the extremeness of this year's event, with a return time of more than 300 years in today's climate is not just due to the high temperatures (which have a return time of 75 years), but also high wind speeds and, in the most impacted regions, unusually low humidity. The fact that the models also show a much lower increase in temperature compared to observations suggests that the synthesised results are indeed conservative as no interdecadal natural variability is expected in temperature, and there is a known underestimation of temperature changes in climate models (van Oldenborgh et al., 2022).

Source		**Probability ratio (95% CI)**	**Intensity change (°C) (95% CI)**
Reanalysis	**Past- Present**	**∞ (12.1, ∞)**	**3.7 (1.8, 5.5)**
Models		22.5 (0.08, 168000)	**1.1 (0.17, 2.0)**
Synthesis		-	**1.6 (0.45, 2.8)**
Models only	**Future**	**6.6 (3.4, 14.4)**	**1.3 (0.8, 1.8)**

Table 6.2: *Summary of synthesised changes in TX5x, presented in Figures 6.3 and 6.4. Statistically significant changes are highlighted in* ***bold****.*

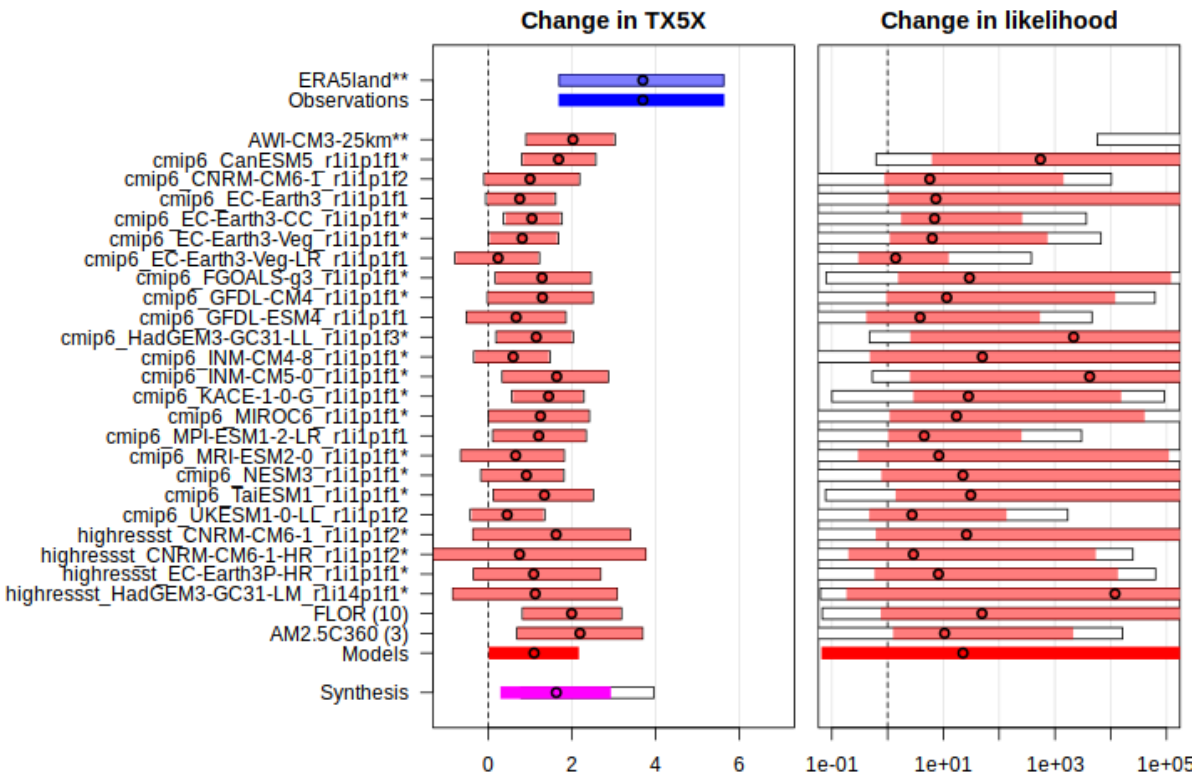

Figure 6.3: *Synthesis of (left) probability ratios and (right) relative intensity changes when comparing the return period and magnitudes of Tx5x in South Korea between the current climate and a 1.3°C cooler climate. For rows marked with * the upper bound of the probability ratio was originally infinite and was inferred; for rows marked with ** both the best estimate and the upper bound were inferred. Because no data were available to infer the central and upper limits for the observational products, no synthesis could be carried out in this case.*

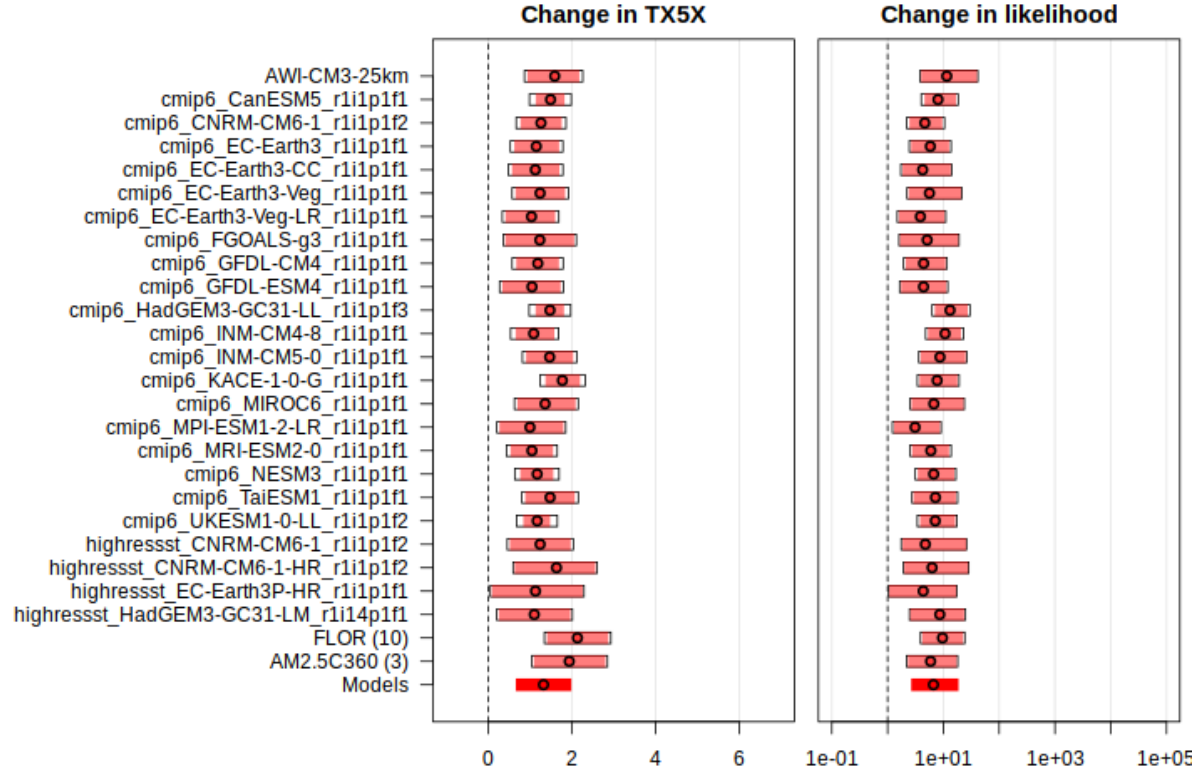

Figure 6.4: *As Figure 6.2, synthesising changes in TX5x between the current climate and a 1.3°C warmer climate (that is, a climate that is 2.6°C warmer than preindustrial).*

6.3 PR-FM

For the last event definition analysed, rainfall in February and March, we find no attributable signal due to climate change. While the observations do show a weak drying trend, climate models do not reproduce this but simulate a different responses to global warming, with the overall synthesised result centred around no change both for the past-to-present (Figure 6.5) as well as the present-to-future analysis (Figure 6.6). This may be due to Korea's complex geography as a relatively small landmass surrounded by ocean, and is known to experience long-term decadal variability. While we cannot attribute the observed drying in this study, it is important to take the possibility of a drying into account for adaptation planning as it would increase the fire risk further than suggested by the analysis of HDWI5x alone.

Source		**Probability ratio (95% CI)**	**Intensity change (%) (95% CI)**
Reanalysis	**Past- Present**	1.53 (0.48, 3.88)	-11.6 (-33.2, 21.1)
Models		0.88 (0.31, 3.04)	1.67 (-29.3, 45.1)
Synthesis		1.19 (0.39, 3.51)	-6.44 (-31.8, 30.4)
Models only	**Future**	0.77 (0.54, 1.05)	7.91 (-1.19, 15.5)

Table 6.3: *Summary of synthesised changes in PR-FM, presented in Figures 6.5 and 6.5. Statistically significant changes are highlighted in* ***bold****.*

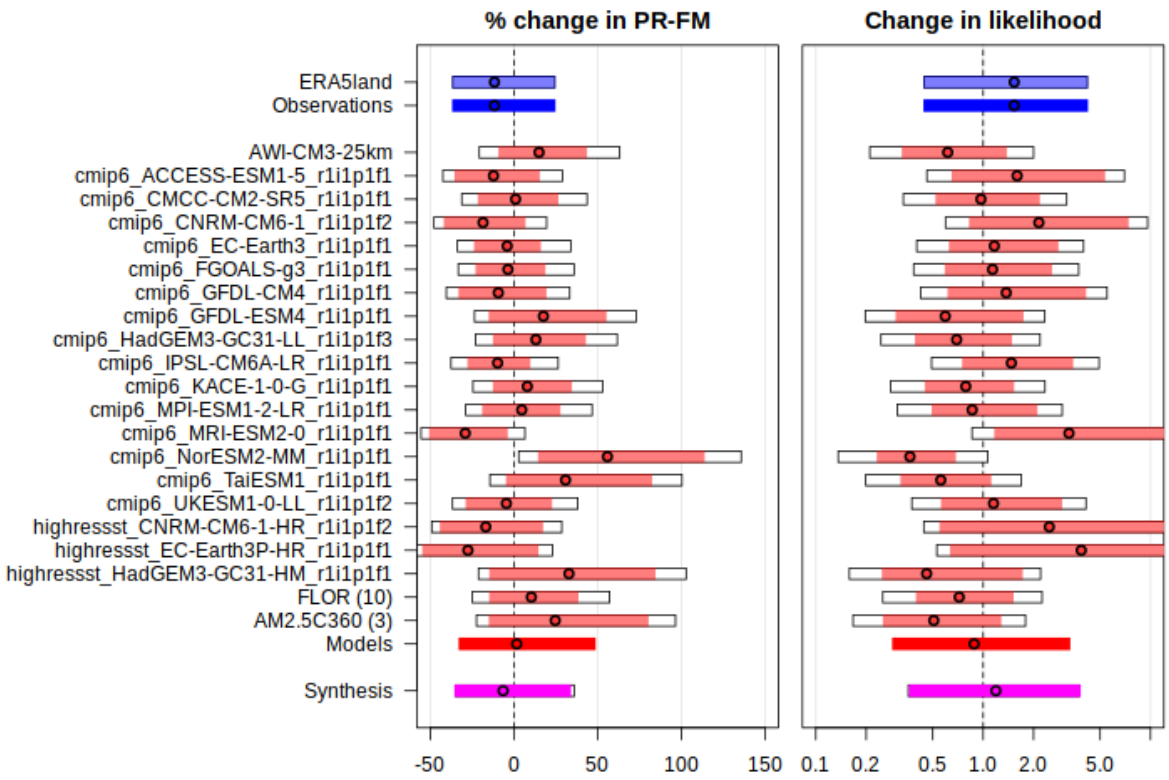

Figure 6.5: *Synthesis of (left) probability ratios and (right) relative intensity changes when comparing the return period and magnitudes of PR-FM in South Korea between the current climate and a 1.3°C cooler climate.*

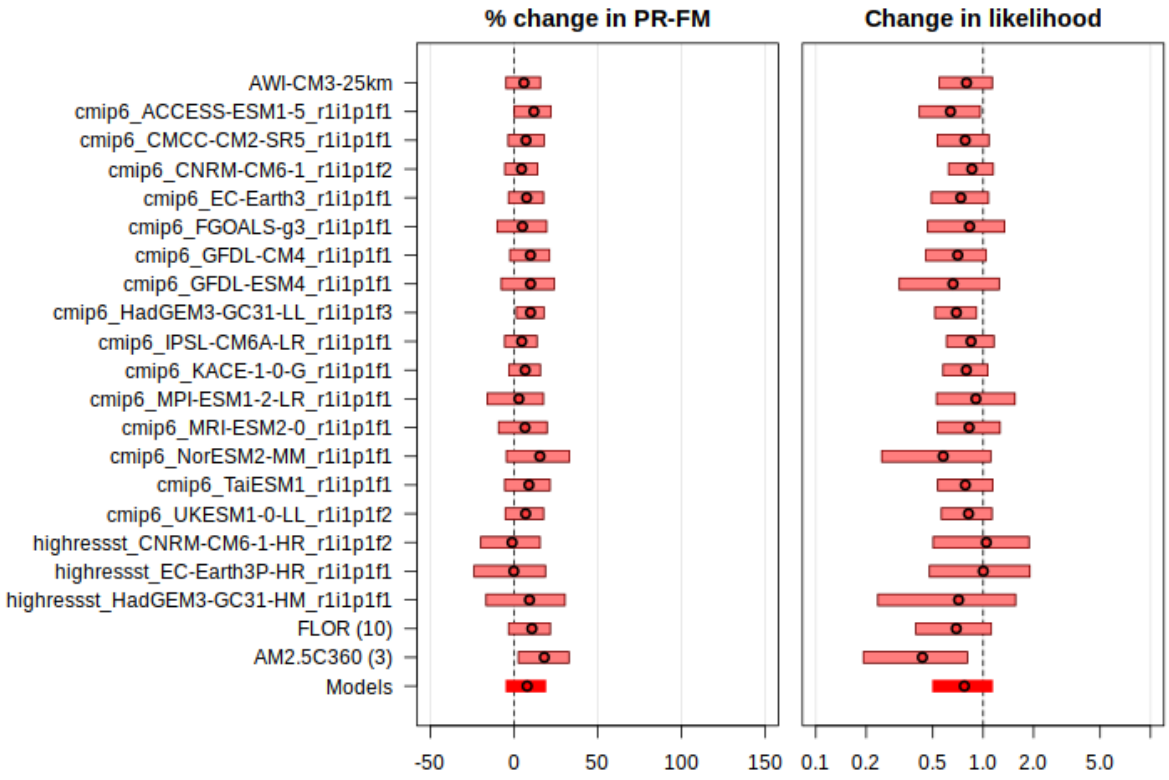

Figure 6.6: *As Figure 6.5, synthesising relative changes in PR-FM between the current climate and a 1.3°C warmer climate (that is, a climate that is 2.6°C warmer than preindustrial).*

7 Vulnerability and exposure

In March 2025, southeastern South Korea experienced its most devastating wildfire season on record. Between March 22 and 23, multiple fires ignited and spread rapidly, engulfing vast areas in the days that followed. The blazes claimed 32 lives (the majority of whom were in their 60s and 70s as well as people with mobility-impairments), injured 45, displaced approximately 37,000 people from their homes, damaged about 5,000 structures, and burned more than 100,000 hectares, making them South Korea's largest on record (AFP, 2025; McGrath, 2025; National Human Rights Commission of Korea, 2025). Eastern South Korea is defined by rugged mountains, including the Taebaek and Sobaek ranges, and a mosaic of wildland-urban interfaces. It is home to some of the country's most critical industrial assets: Busan, one of the world's busiest container ports; Ulsan, a global hub for shipbuilding, automotive manufacturing, and petrochemicals; and Daegu, a centre for high-tech textiles and logistics. These industrial corridors are increasingly exposed to environmental shocks, including wildfire-related disruptions to supply chains, transport networks, and energy infrastructure.

South Korea is accustomed to wildfires, which occur annually in spring. Before this year, the two large wildfires were the 2000 Goseong fire, notable for its expansive burn area (more than 23,000 hectares), and the 2022 Uljin-Samcheok fire, which broke out unusually early in the season, persisted for 213 hours, and threatened critical infrastructure, prompting large-scale emergency response (Chang et al., 2024; Park et al., 2023). Since 2000, at least 33 large-scale wildfires have occurred in South Korea, with fire seasons lengthening by 25 days and shifting spatially toward northeastern and inland regions, including the Gyeongsangbuk Province (Kim et al., 2025; Kwon, 2018).

In this analysis, we examine the underlying factors that shaped the 2025 events, focusing on the socio-ecological landscape, institutional architecture, and evolving practices of risk anticipation and management.

7.1 Intersecting Risks at the Wildland-Human Interface

The fires disproportionately affected rural and peri-urban populations, particularly in wildland-urban interface (WUI) zones; transitional areas where human development meets undeveloped wildland vegetation, posing heightened risks of wildfire exposure. These zones also contain high-value assets, including national energy infrastructure, ports, and industrial corridors in Ulsan and Busan, which are increasingly vulnerable to cascading disruptions from wildfire, as seen in past near-miss events involving liquefied natural gas (LGN) and nuclear facilities, used to store and distribute gas for national energy supply and generate electricity for millions (Park et al., 2023). In the 2025 event, Uiseong, one of the hardest-hit areas, saw the destruction of Gounsa Temple - originally built in 618 AD - and damage to 30 registered cultural heritage sites, including relics from the Joseon Dynasty (AFP, 2025; Sang-Soo, 2025). These losses, sites of profound historical and spiritual significance, constitute a significant disruption to the region's cultural fabric and communal life. Beyond the destruction of heritage structures, the fires have disrupted local religious practices, affected community cohesion, and poses lasting economic challenges due to diminished tourism. With at least 19% of the country's over 900 temples nestled in the Baekdudaegan mountain range along the east

coast, a significant share of South Korea's cultural heritage remains exposed to wildfire (National Atlas, 2020).

South Korea is over 62% forested, with significant tree cover concentrated in its eastern coastal and mountainous regions. The ecological composition of these forests plays a critical role in wildfire behavior. Notably, around 11% of South Korea's forested areas fall within WUI zones. These areas are particularly susceptible to ignition and have accounted for nearly 30% of wildfires recorded between 2016 and 2022 (Jo et al., 2023). As these zones continue to expand (Jo et al., 2023), in addition to the intensification of fire weather conditions, so too does the complexity of managing fire risks at the intersection of ecological and human systems.

Compounding this ecological vulnerability are legacies of land use and forest management. Reforestation campaigns since the 1970s have increased fuel loads in some reforested regions, especially in provinces like Gangwon and Gyeongsangbuk, heightening fire risk (Kim et al., 2025). Human activity remains the leading ignition source: 49% of wildfires are caused by human error, followed by agricultural burning and smoking (Korea Forest Service, 2022 in Kim et al., 2025). While an ignition source is necessary for a wildfire occurrence, for the extremely large and damaging wildfires seen this March, continuous vegetation and extreme fire weather conditions are also necessary.

The timing of the fires, March through May, coincides with South Korea's fire season, driven by dry foehn winds and low spring humidity. As climate change accelerates shifts in fire-prone areas, approximately 6.5% of national territory is already categorized as high-risk, underscoring the need for adaptive land-use planning and integrated forest management strategies (Choi & Chae, 2025).

The scale and severity of human and ecological exposure in the 2025 wildfires reflect not only the increasing intensity of climatic and environmental conditions, but also the challenges of managing these risks in landscapes shaped by development, infrastructure, demographic change, and cultural heritage. Understanding who and what is at risk provides a critical foundation for reflecting on how existing policy and planning frameworks are evolving in response to these dynamics, and how emerging lessons from recent events may help inform future efforts to further strengthen resilience.

7.2 The Governance of Wildfire Risk

General safety legislation in South Korea covers important components such as the Occupational Safety and Health Law and the High-Pressure Gas Law, which require hazard assessments for facilities handling dangerous materials. However, these regulations do not currently mandate wildfire-specific risk evaluations, even in regions with known exposure (Park et al., 2023).

The Korea Forest Service (KFS) serves as the lead agency for wildfire detection and suppression in forested and uninhabited areas. In the aftermath of the 2000 East Coast fires, the KFS expanded its operational capacity to include large-scale aerial firefighting and invested in improved early warning systems. These now incorporate real-time indices informed by vegetation, topography, and weather conditions (Han, 2021). These measures, implemented alongside surveillance and fuel management strategies, have been credited with containing fire spread in many recent cases. Despite an increase in

the number of fire incidents, the total burned areas has not shown a statistically significant upward trend - suggesting the effectiveness of suppression efforts (Kim et al., 2025). Nevertheless, the lengthening of the fire season - from 145 to 169 days during 1991-2020 - has intensified demands on suppression resources and monitoring infrastructure. This temporal shift underscores the need for ongoing adaptation within institutional planning cycles.

While these advancements represent significant progress, wildfires are not yet systematically integrated into broader critical infrastructure and national disaster frameworks (Park et al., 2023). In 2022, South Korea narrowly avoided a major Natech disaster - a technological accident triggered by a natural hazard - when wildfires came within 1.2 km of critical energy infrastructure. While no damage occurred, the incident underscores the urgent need for integrated wildfire-specific Natech risk management. Observations from recent wildfire events suggest that jurisdictional boundaries between national agencies, local governments, and infrastructure operators may at times complicate coordinated response efforts in high-risk areas (Park et al., 2023). Strengthening interagency mechanisms may offer opportunities to enhance preparedness and reduce systemic vulnerabilities.

While recent legislative and operational advancements have enhanced South Korea's capacity for fire detection and suppression, many of these measures are oriented toward response rather than long-term adaptation. As fire seasons become longer and more variable, institutions may face growing demands to manage not only fire outbreaks but also their broader economic and social consequences. Ensuring that wildfire preparedness is systematically integrated into infrastructure planning, social protection, and land-use policy could strengthen resilience across sectors. Continued investment in adaptive capacity - including institutional learning, cross-sector coordination, and anticipatory planning - will be essential in navigating an increasingly dynamic risk environment.

7.3 Managing Fire in a Changing Climate

South Korea's wildfire management system features a combination of real-time monitoring, predictive modeling, and aerial suppression capacity. The Korea Forest Service (KFS) leads early detection and rapid response efforts in forested and mountainous areas, supported by local and national firefighting resources. These systems, expanded significantly after the 2000 East Coast fires, include helicopter fleets and high-resolution fire danger indices (Kim et al., 2025). Short-term forest fire outlooks are updated every three hours using real-time meteorological and vegetation data (Jo et al., 2023).

Advanced models such as FLAM and MaxEnt have also been developed to guide long-term forest fire risk assessment and adaptation planning. The FLAM model suggests optimal land management could reduce fire frequency and area burned by up to 70%, while MaxEnt, paired with Shared Socioeconomic Pathway (SSP) scenarios, helps spatially forecast future fire risk (Jo et al., 2023). Economic modeling reinforces this preventive emphasis: projections indicate wildfire damage could reduce regional GDP by as much as 1.23%, particularly in the industrialized east (Kim & Kwon, 2023).

Despite these capabilities, persistent gaps remain. Coordination and risk communication are uneven - particularly in industrial zones, where some private operators conduct risk assessments, but national enforcement and standardization are limited (Park et al., 2023).

The 2025 wildfires exposed the limits of this system under compounding stressors - drought, wind, and terrain. Fires ignited on a Friday and escalated quickly, with 30 separate incidents reported nationwide. In response, the national fire agency raised the emergency status to its highest level by the following Tuesday. Containment and suppression extended over ten days and involved thousands of emergency personnel, including about 5,000 military members and aerial assets - among them helicopters from the US military (Lee, Kim & Lee, 2025).

The most extensive blaze occurred in Uiseong, affecting over 45,000 hectares. Although initially reported extinguished, it reignited the following evening. A second major fire in Sancheong was also brought under control (McGrath, 2025). Several provinces were designated disaster zones, and the KFS extended its highest fire warning to cover the entire country (Hubenko, 2025; Lee, 2025).

However, the crisis revealed serious operational constraints. Strong winds, along with the fatal crash of a firefighting aircraft, forced authorities to suspend aerial operations - highlighting the vulnerability of the suppression system when faced with extreme conditions. Further, evacuation efforts were hampered by guidance and alerts which were reported to be unclear and inconsistent. Some alerts were reported to lack information on the locations of evacuation centres, which in some cases may have complicated efforts to reach safety (McGrath, 2025). Further, according to an official, evacuation sites had to be revised frequently as the wildfire situation evolved rapidly. Elderly residents, in particular, encountered significant obstacles; although disaster alerts were sent via text message, many were unable to evacuate independently due to mobility issues or other limitations (Se-Jin, 2025). This disconnect between predictive tools and last-mile communication underscores the need for improved public guidance systems, especially for populations with constrained mobility.

Governors of North and South Gyeongsang Provinces, respectively, stated that firefighters were not adequately equipped or supported to respond effectively to the fires (McGrath, 2025). In response to the crisis, the government pledged to strengthen enforcement measures against illegal burning, identified as a major cause of wildfires, and to take stronger action against individual negligence (Lee, Kim & Lee, 2025). Future strategies must integrate forecasting, land-use planning, communication reform, and economic resilience frameworks (Jo et al., 2023; Park et al., 2023; Kim & Kwon, 2023).

These systemic challenges, from aerial suppression limits to communication inadequacies, highlight that even advanced fire management systems can face strain when confronted with fast-moving, large-scale wildfires. In such scenarios, full containment may be infeasible, shifting the focus toward protecting critical assets and lives. This underscores the vital importance of pre-fire preparation, including proactive fuel management, structural hardening, and well-practiced evacuation procedures. In the broader climatological context, explored in the attribution analysis, these lessons point to the need for strengthened, anticipatory risk preparedness and resilience strategies.

V&E conclusions

The 2025 wildfires in South Korea occurred under fire weather conditions made approximately twice as likely, and about 15% more intense, by human-induced climate change. These unprecedented conditions exposed the limits of even well-developed suppression systems. With fires increasingly likely to exceed control capacity, the emphasis must shift toward proactive risk reduction, particularly in the growing wildland-urban interface (WUI) zones where industrial, residential, and cultural assets converge.

Adaptation efforts will require systematic integration of wildfire preparedness into infrastructure development, land-use planning, and social protection frameworks. This includes managing forest fuel loads, reinforcing critical infrastructure, expanding tailored early warning systems, and designing inclusive evacuation protocols, especially for at-risk groups such as older adults and those with limited mobility. As climate change accelerates, enhancing adaptive capacity across sectors will be essential to reduce harm from intensifying wildfire risks.

Funding Statement

CB was supported by the European Commission Horizon 2020 Programme (Grant No. 7654321).

JYL and YWS were supported by the Institute for Basic Science (IBS) IBS-R028-D1. JYL, YMY, and JEY were supported by the National Research Foundation of Korea (NRF) grant funded by the Korea government (MSIT) (No. RS-2024-00416848).

Data availability

All time series used in the attribution analysis are available via KNMI's Climate Explorer.

References

All references are given as hyperlinks in the text.

Appendix

A.1 Spatial pattern of fitted trends

HDWI5x was extreme across the whole of South Korea in March 2025 (Figure A1.1b); the upward trend is also relatively homogeneous across most of the country (panels c and d).The spatial pattern is very similar to the pattern of changes in temperature (Figure A1.2).

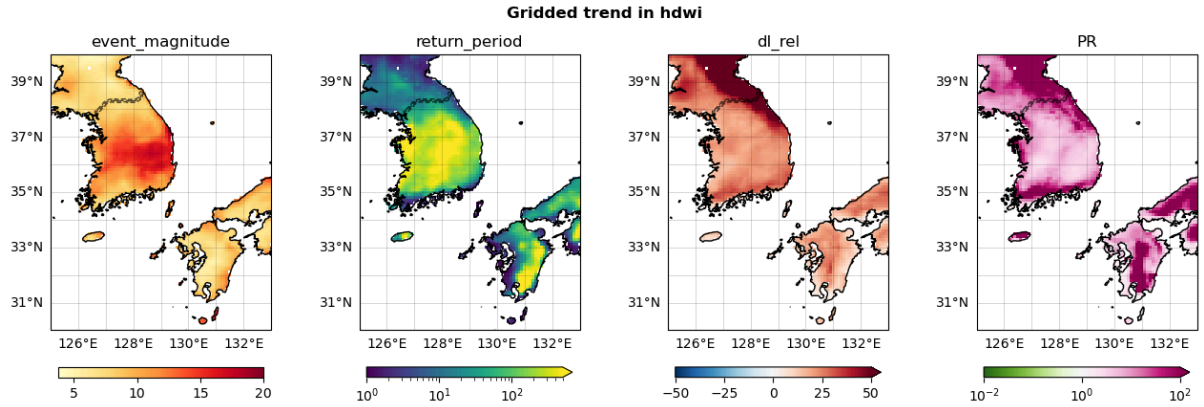

Figure A1.1: *Maps of statistical model fitted at each grid cell independently (ERA5-land).* ***(a)*** *Maximum 5-day HDWI during March 2025;* ***(b)*** *estimated return period;* ***(c)*** *% change in HDWI5x associated with 1.3C increase in GMST;* ***(d)*** *probability ratio (change in likelihood) of the observed event associated with 1.3C increase in GMST.*

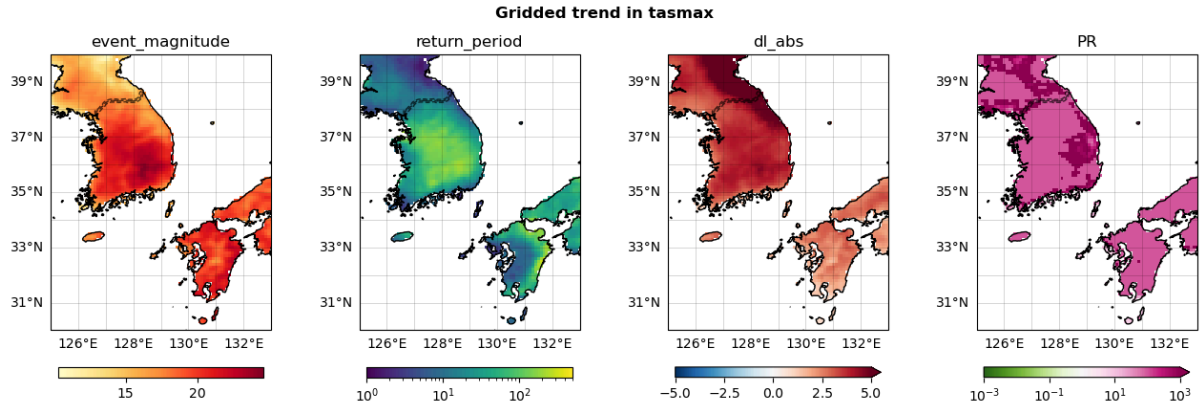

Figure A1.2: *Maps of statistical model fitted at each grid cell independently (ERA5-land).* ***(a)*** *Maximum 5-day TX during March 2025;* ***(b)*** *estimated return period;* ***(c)*** *Change in TX5x associated with 1.3C increase in GMST (degC);* ***(d)*** *probability ratio (change in likelihood) of the observed event associated with 1.3C increase in GMST.*

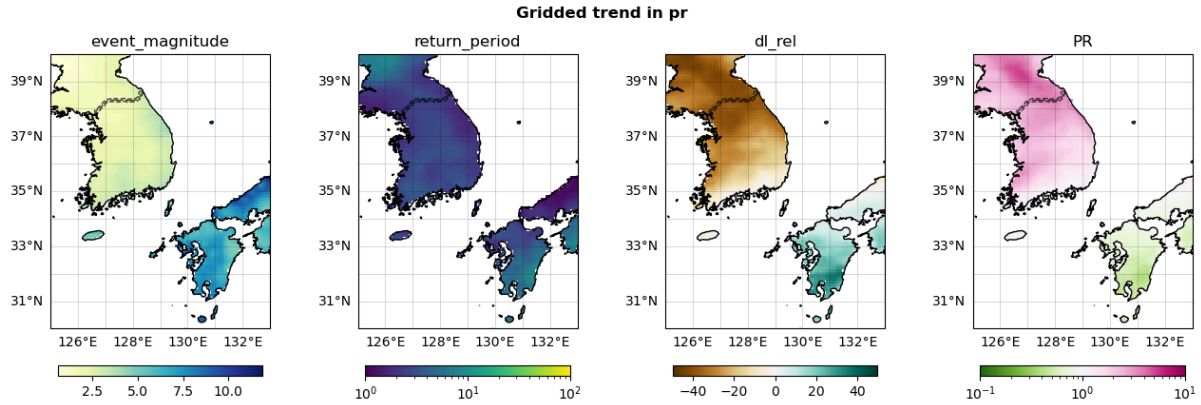

Figure A1.3: *Maps of statistical model fitted at each grid cell independently (ERA5-land).* ***(a)*** *February-March 2025;* ***(b)*** *estimated return period;* ***(c)*** *Change in PR-FM associated with 1.3C increase in GMST (degC);* ***(d)*** *probability ratio (change in likelihood) of the observed event associated with 1.3C increase in GMST.*

A.2 Trends in stations vs ERA5-land

Station name	Latitude	Longitude	Years	Excluded?
Ulleungdo	37.48	130.90	1938 - 2025	Not on mainland
Uljin	36.99	129.41	1971 - 2025	
Andong	36.57	128.71	1973 - 2025	
Sangju	36.41	128.16	**2002** - 2025	Short time series
Pohang	36.03	129.38	1949 - 2025	
Bonghwa	36.94	128.91	**1988** - 2025	Short time series
Yeongju	36.87	128.52	1972 - 2025	
Mungyeong	36.63	128.15	1972 - 2025	
Cheongsong	36.44	129.04	**2010** - 2025	Short time series
Yeongdeok	36.53	129.41	1972 - 2025	
Uiseong	36.36	128.69	1973 - 2025	
Gumi	36.13	128.32	1973 - 2025	
Yeongcheon	35.98	128.95	1972 - 2025	
Gyeongju	35.82	129.20	**2010** - 2025	Short time series

Table A.2.1: *List of stations in the affected region with all HDWI sub-indices available, with coordinates and length of time series.*

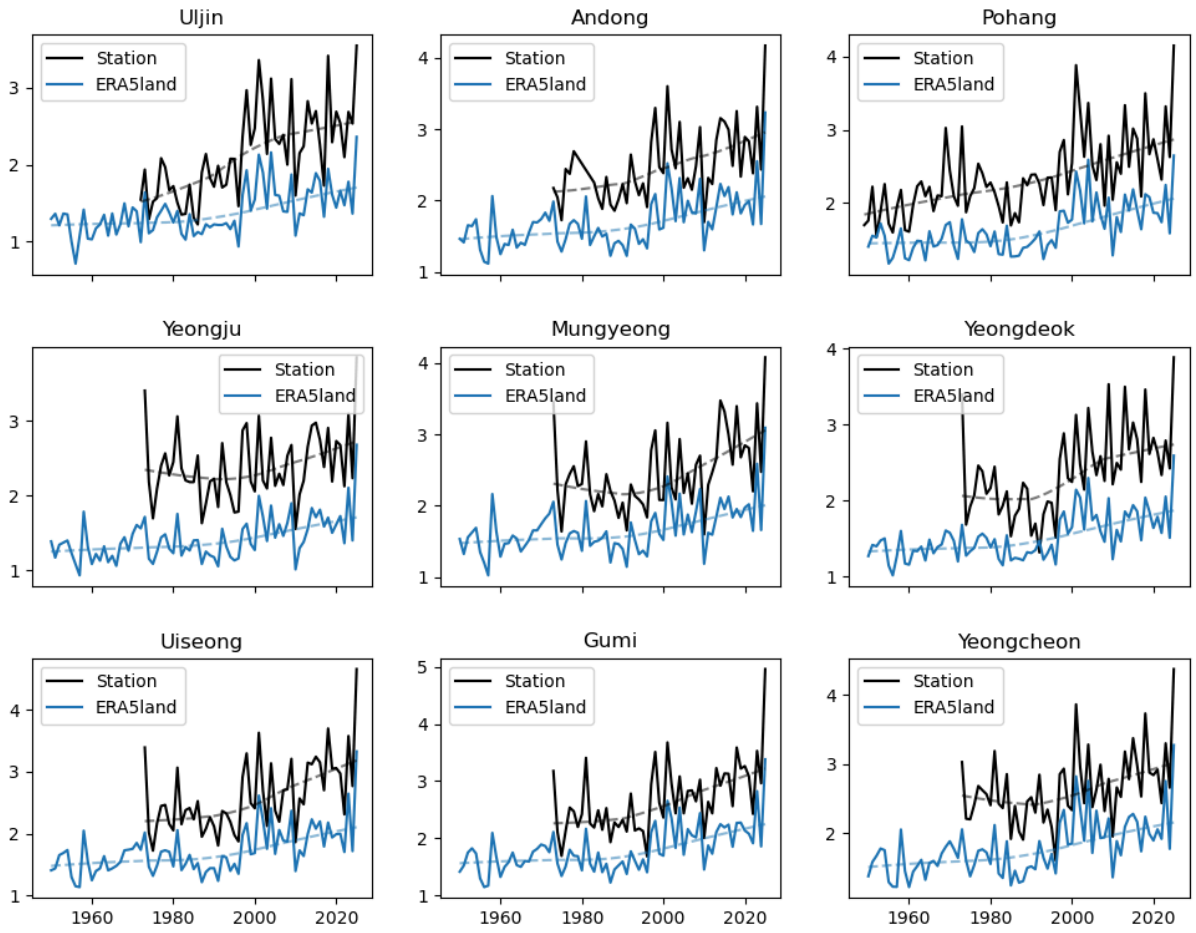

Figure A2.1: *Time series of VPD5x (March maximum of 5-day averaged VPD) at nine stations (black) and from the nearest grid cell in ERA5-land (blue). Dashed lines represent a nonparametric loess smoother showing the trend over time.*

	% change in HDWI			PR (change in likelihood)		
Station	**est**	**lower**	**upper**	**est**	**lower**	**upper**
Uljin	-3.5	-16.3	15.8	0.82	0.37	2.16
Andong	11.0	3.5	21.5	2.36	1.22	17.1
Pohang	2.6	-5.3	12.4	1.20	0.64	2.25
Yeongju	20.1	5.7	37.0	7.44	1.74	580
Mungyeong	21.7	9.4	40.5	14.2	2.07	4620
Yeongdeok	50.8	35.0	72.3	3.96	2.15	59.1
Uiseong	19.2	9.8	31.7	2.87	1.55	10603
Gumi	-13.0	-20.8	-3.8	0.24	0.00	0.73
Yeongcheon	19.6	9.5	34.0	9.89	1.82	1593
All stations	**12.9**	**-16.9**	**54.6**	**2.22**	**0.12**	**103**

Table A2.2: *Estimated % change in HDWI and likelihood of a similarly extreme March HDWI event, with overall synthesised average (bottom row).*

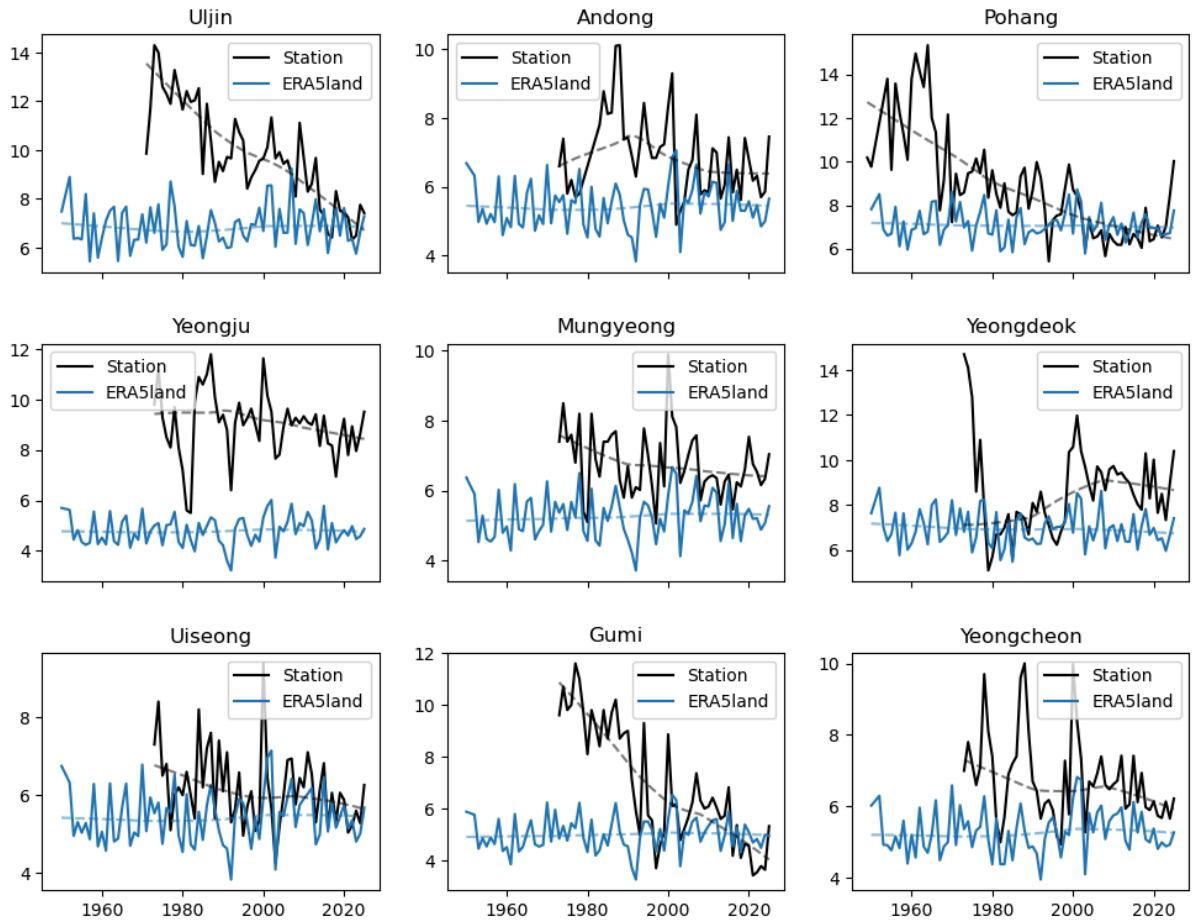

Figure A2.2: *Time series of sfcWindmax5x (March maximum of 5-day averaged daily maximum sustained wind speed) at nine stations (black) and from the nearest grid cell in ERA5-land (blue). Dashed lines represent a nonparametric loess smoother showing the trend over time.*

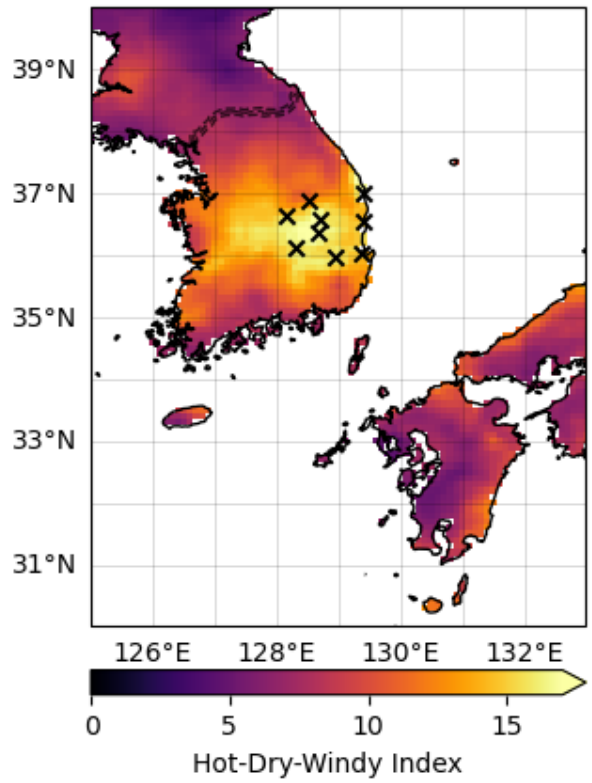

***Figure A2.3**: As Figure 1.1a, with locations of stations marked with X.*

A.3 Trends in February-March precipitation

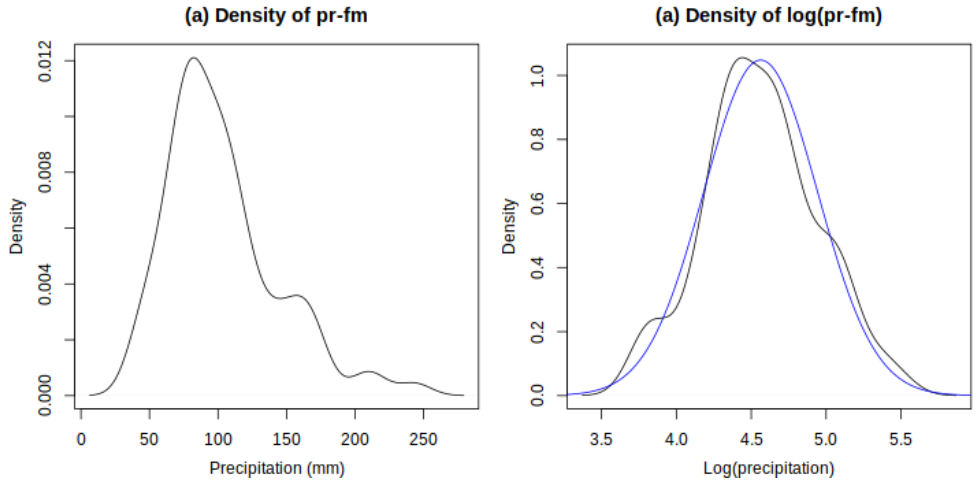

Figure A3.1:

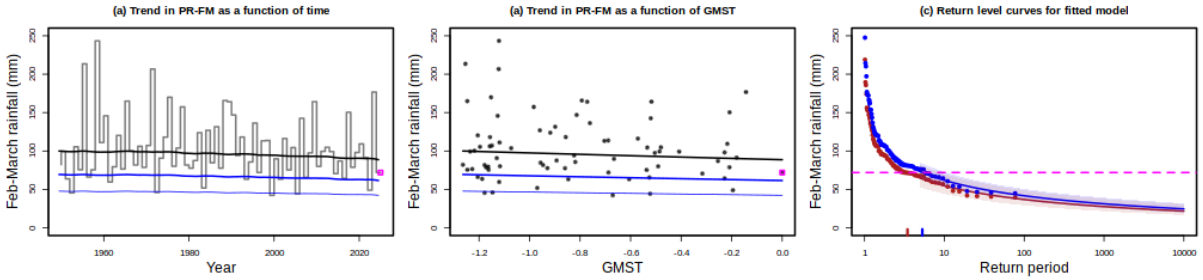

Figure A3.2: *As figure 3.6, but without log transformation.*

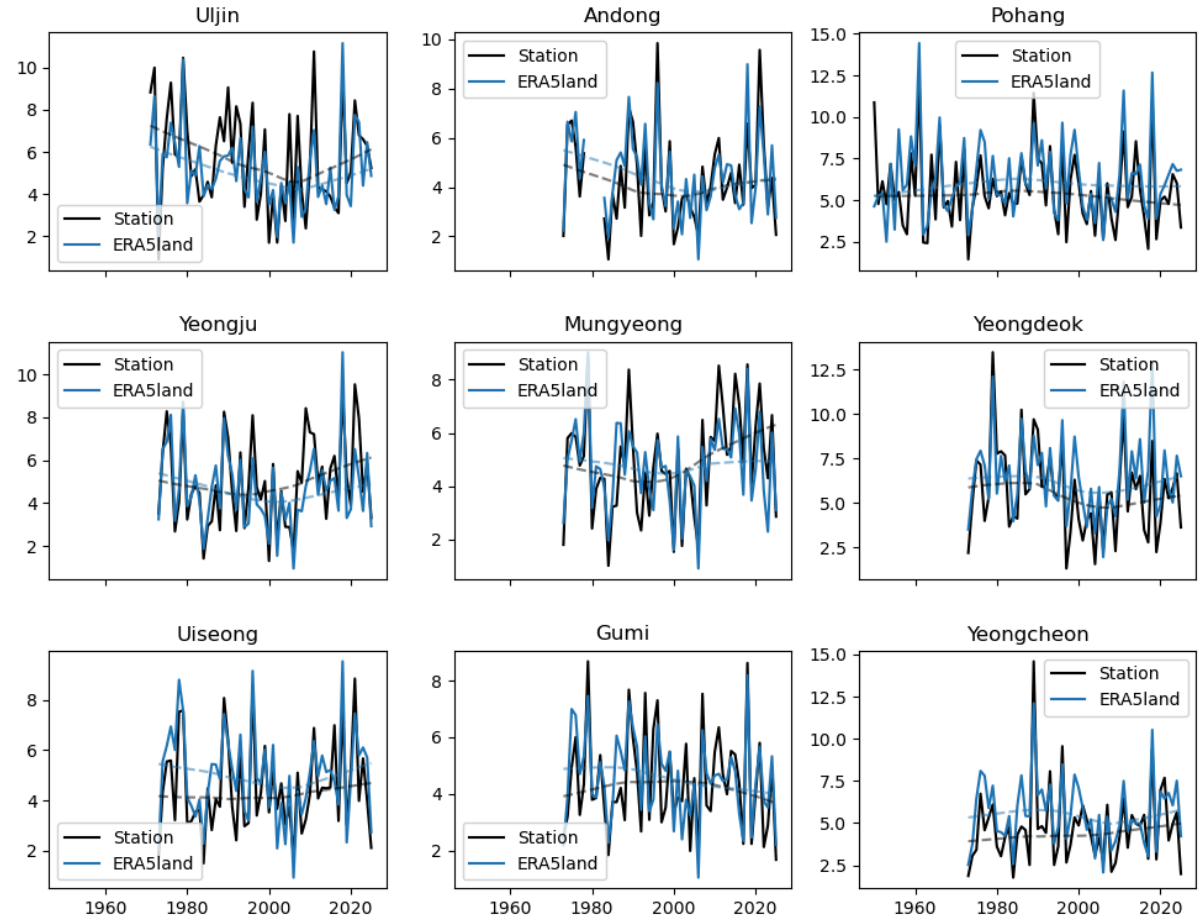

Figure A3.3: *Time series of mean February-March rainfall rates on days on which rainfall was recorded at the station (black) and from the nearest grid cell in ERA5-land (blue). Dashed lines represent a nonparametric loess smoother showing the trend over time.*

A.4 Seasonal cycles used in model evaluation

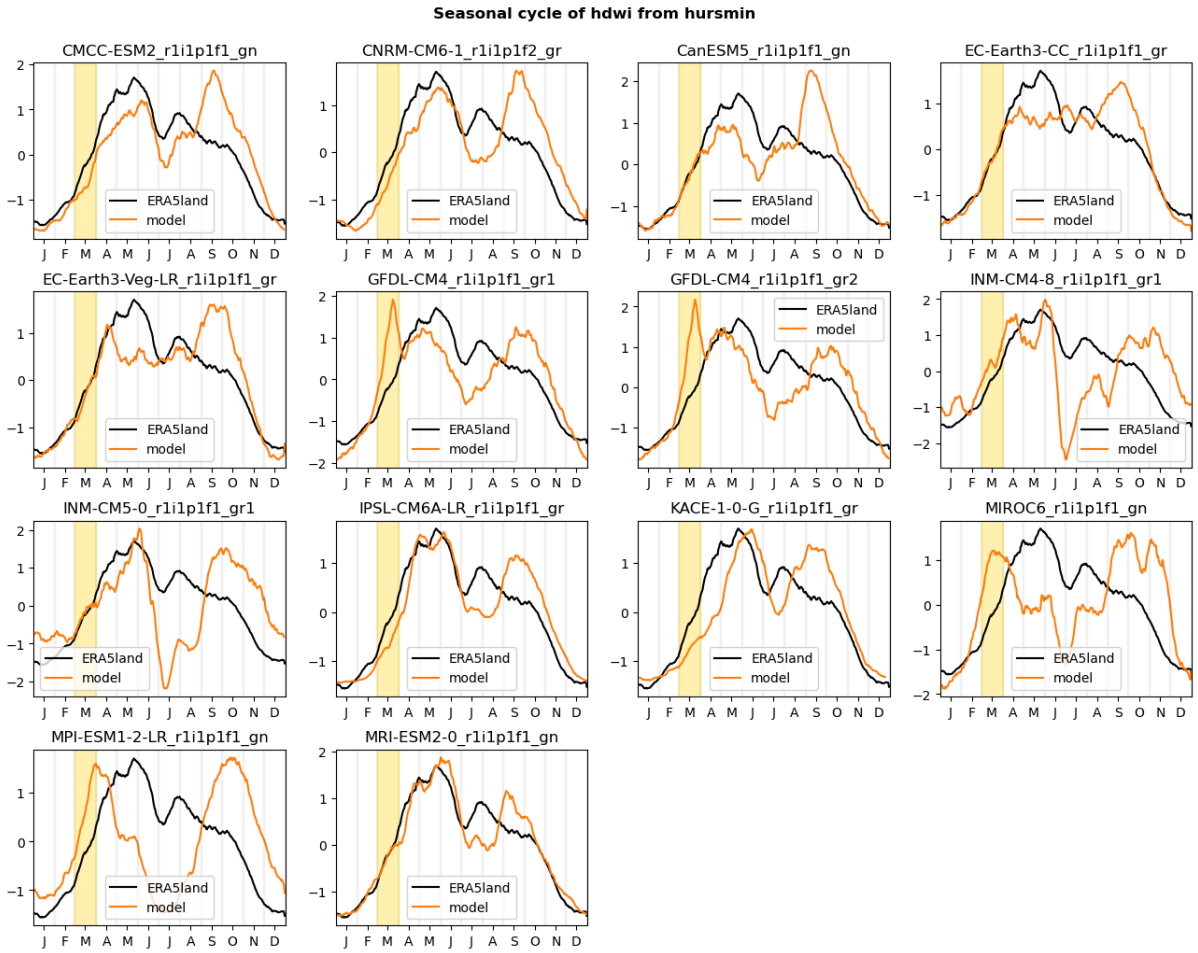

Figure A4.1: *Seasonal cycle of HDWI (scaled to have zero mean and variance 1) over South Korea, used in model evaluation - CMIP6.*

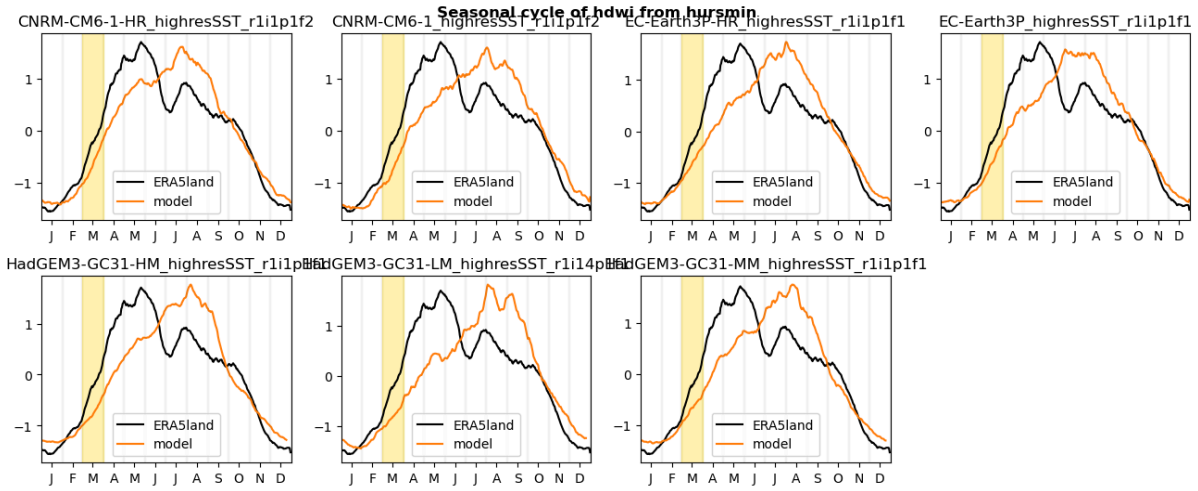

Figure A4.2: *Seasonal cycle of HDWI (scaled to have zero mean and variance 1) over South Korea, used in model evaluation - HighResMIP*

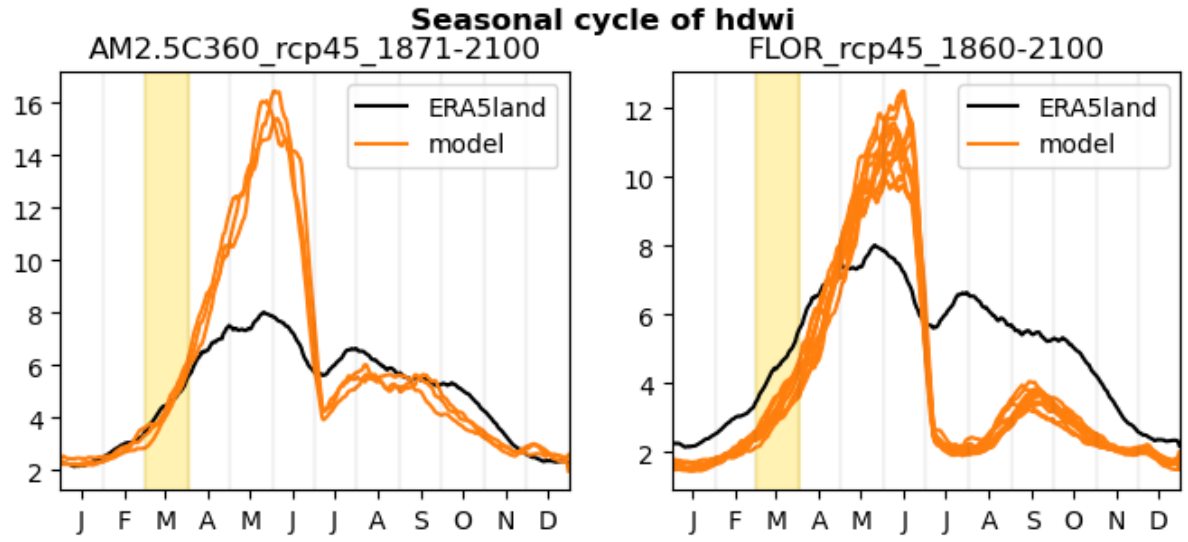

Figure A4.3: *Seasonal cycle of HDWI (scaled to have zero mean and variance 1) over South Korea, used in model evaluation - FLOR / AM2.5 / AWI-CM3*

Seasonal cycle of pr

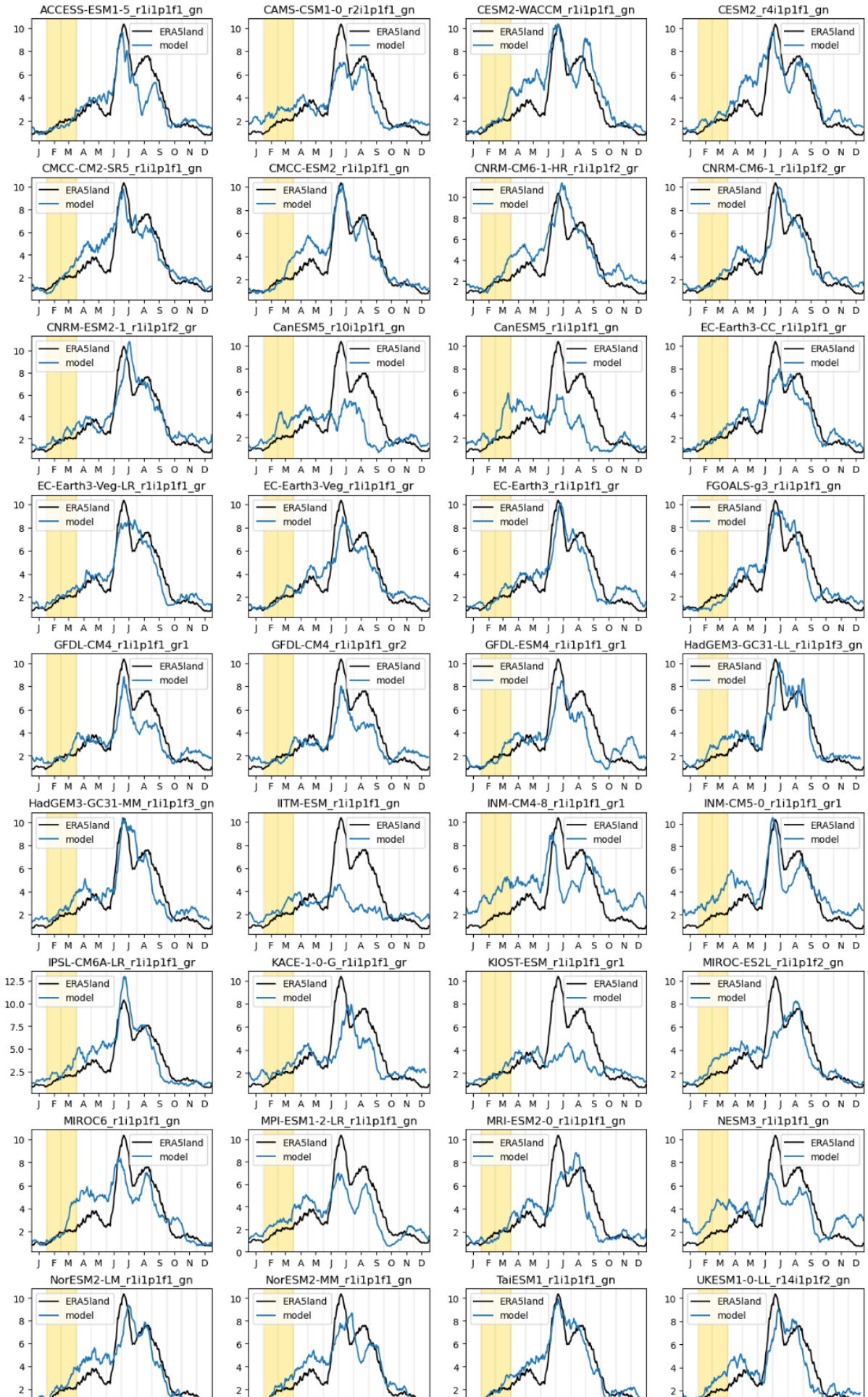

Figure A4.4: *Seasonal cycle of precipitation used in model evaluation over South Korea, - CMIP6*

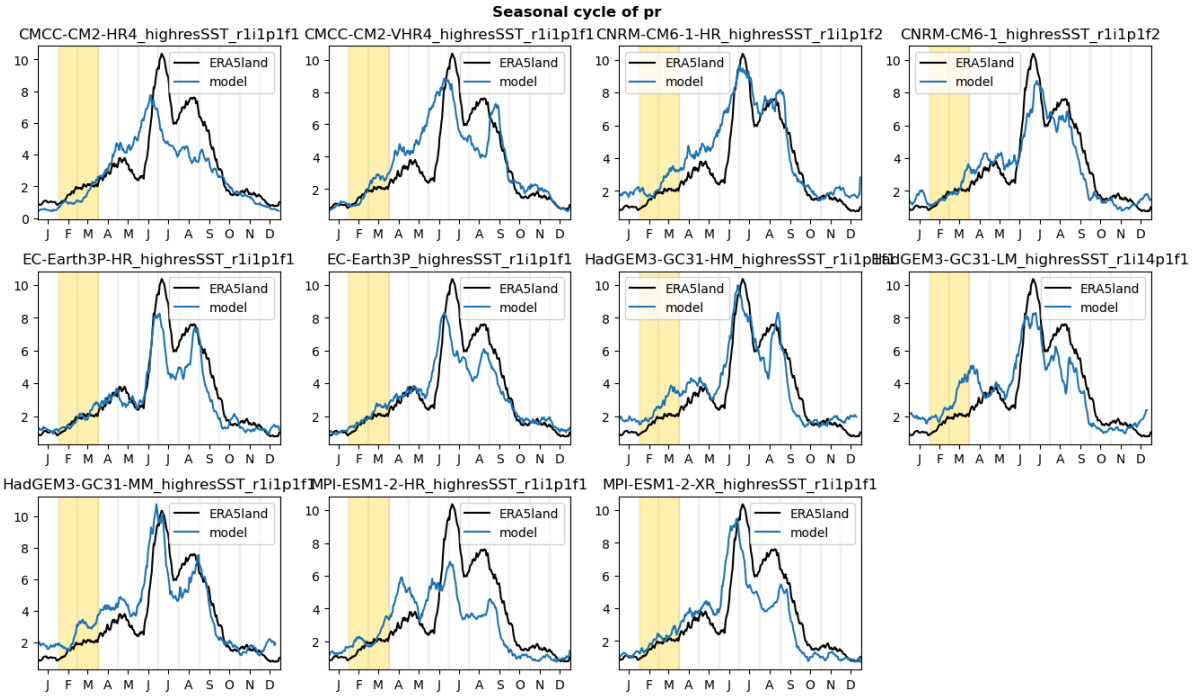

Figure A4.5: *Seasonal cycle of precipitation over South Korea, used in model evaluation - HighResMIP*

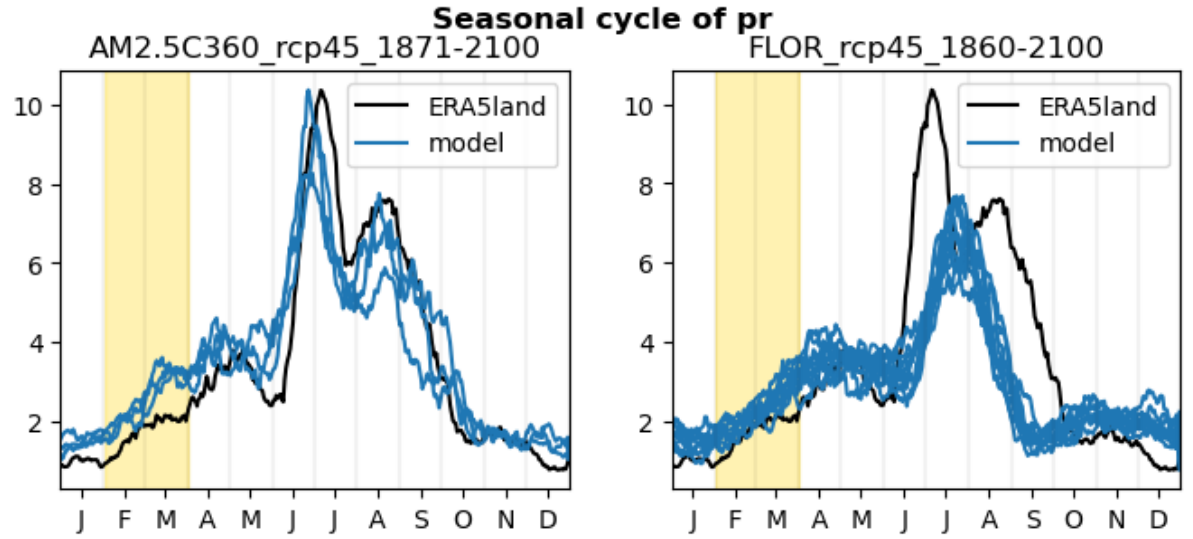

Figure A4.6: *Seasonal cycle of precipitation over South Korea, used in model evaluation - FLOR / AM2.5*

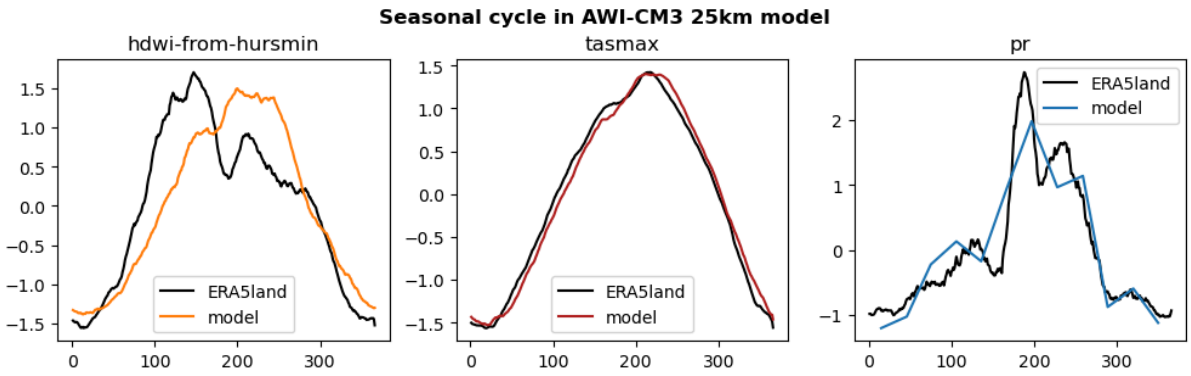

Figure A4.7: *Seasonal cycle of HDWI, daily maximum temperatures and precipitation over South Korea (all scaled to have zero mean and unit standard deviation for easier comparison), used in model evaluation - AWI-CM3*